THE APPLICATION OF LOW ENERGY PHOTON IONIZATION TO HETEROGENEOUS AEROSOL CHEMISTRY

David Gerald Nash

A dissertation submitted to the faculty of the University of North Carolina at Chapel Hill in partial fulfillment of the requirements for the degree of Doctor of Philosophy in the Department of Chemistry

Chapel Hill

2006

Approved by:

Tomas Baer

Richard Kamens

Gary Glish

ABSTRACT

David G. Nash: The Application of low energy photon ionization to heterogeneous aerosol chemistry

(Under the direction of Tomas Baer)

The first part of this dissertation is a review of developments made in the field of aerosol mass spectrometry. The focus of the research is on the reduction of fragmentation observed in the mass spectra of organic molecules and its application to studying the reactivity of more realistic aerosol particles. Initial studies examined reduction in oleic acid fragmentation with lower energy (8.75 eV) photons generated using resonance difference frequency mixing (RDFM), a form of four wave mixing. In the same study, the effects of different particle vaporization methods on the ion production mechanism are discussed. Understanding both of these issues is very important to accurate kinetics studies.

These findings were then applied to the study of the reactivity of mixed myristic acid/oleic acid particles. While still not as complex as typical atmospheric particles, studying particles consisting of a binary mixture, especially the ones studied here which can undergo phase changes with changing relative composition is an important first step in understanding issues such as why the lifetime of oleic acid as measured in the field is longer than what would be predicted from laboratory studies. Our study of mixed particles demonstrates reduced reactivity upon crystallization of myristic acid.

Possibilities for the way in which crystallization would have to occur to result in the observed degree of decreased reactivity are also discussed. .

ACKNOWLEDGEMENTS

First, I would like to thank Dr. Tomas Baer for all the guidance he has given me over my time at UNC. Tom was always willing teach, and his enthusiasm for it was invaluable. Furthermore, Tom was instrumental in teaching me to learn, to think scientifically and to always ask questions. I would also like to thank Dr. Ephraim Woods and Dr. Geoff Smith. Though the time we overlapped was short, I learned so much from both of them. Also, since they have left, both have always been available and eager to continue to help. Dr. Michael Tolocka has also been instrumental in my educational experience. He has helped me to better understand the approach necessary for studying aerosols. Dr. Tolocka was also integral in helping me to sustain the drive to be my best.

I would also like to acknowledge Jared Paul, David Slade, and Aaron and Ginger Rothrock for all the help and support they have shown me over the years. Finally, I would like to thank my parents. They have been there every step of the way and have always done anything and everything they could to make sure I succeeded.

TABLE OF CONTENTS

Page

LIST OF FIGURES

CHAPTER 1

Aerosol Mass Spectrometry: An Introductory Review

Aerosol mass spectrometry has become an essential tool in monitoring tropospheric aerosols. Various approaches have been developed for analyzing particles that range in size from 10 nm to 10 μm in diameter, and which consist of salts, soot, crustal matter, metals, and organic molecules, often all mixed together. This wide variety of particles has generated an equally wide variety of ionization sources, which include electron impact, laser ionization, laser desorption, chemical ionization, and electron capture ionization. Some instruments are capable of single particle analysis, while others require the collection of an ensemble of particles to obtain sufficient sample for analysis. Most instruments have been designed to ionize and analyze particular classes of compounds (e.g. salts, soot, or organics). This introduction provides a very broad overview of the aerosol mass spectrometry field.

1.1 Introduction

The field of aerosol mass spectrometry has been reviewed in a number of recent articles and the interested reader is encouraged to consult these.[1,2,3,4,5,6] This chapter serves

as a broad overview to the field. The emphasis here is on various aspects of aerosols, including their transport, light scattering properties, and composition, that affect mass spectrometer design and performance. The ideal aerosol mass spectrometer should be capable of determining the size of an individual aerosol particle, and provide a quantitative measure of each of its molecular constituents. This is a difficult task because atmospheric particles range in size from less than 10 nm to greater than 10 μm, and the molecular constituents are often mixtures that can include sea salt, soot, heavy metals, sand, and a bewildering assortment of organic molecules. The ability to detect individual particles is important in environmental studies where it is essential to know whether particles are uniform mixtures of many constituents, or whether the aerosol is a heterogeneous mixture of various types of particles. Finally, great benefits accrue if such instruments are portable so that they can be transported to various locations. A number of portable instruments have been developed, and some are commercially available. In this chapter, we discuss the fundamental issues associated with aerosol mass spectrometry.

The broad distribution of particle sizes poses a number of challenges in aerosol analysis. For instance, a 10 μm particle contains about 500 pg of material, which is readily within the range of any mass spectrometer's sensitivity. However, the mass drops by nine orders of magnitude when the diameter is reduced by a factor of 1000 to 10 nm.

Molecular identification in single 10 nm particles is clearly beyond the range of current instruments, although atomic constituent analysis in which multiple atomic ions are produced from each molecule may be possible.[7] Other issues include the efficiency of particle introduction into the mass spectrometer, which is readily accomplished with large particles but becomes less efficient with smaller particles.

The distribution of particle sizes in the troposphere is shown in Figure 1.1 in the form of three graphs in which the number concentration, the surface area, and the total mass concentrations of a typical urban aerosol are plotted as a function of the particle diameter.[8]

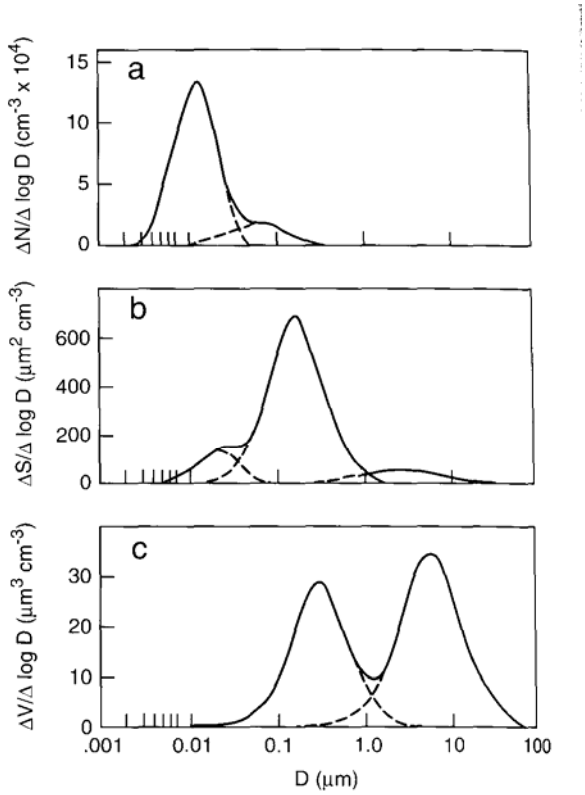

Figure 1.1: A typical urban tropospheric aerosol size distribution, taken with permission from Finlayson-Pitts and Pitts.[8] a) shows the number density distribution, b) the surface area distribution, and c) the volume or mass distribution.

Such distributions are generally plotted as ΔN/ΔlogD vs. log D, where N is the number of particles per unit volume, because the range of sizes from 10 nm to 10 μm spans three orders of magnitude, which would be difficult to plot on a linear scale. The relationship between a standard distribution, N vs. D (ΔN/ΔD vs. D) and a logarithmic distribution (N vs. log D) in which the ordinate is ΔN/ΔlogD, is shown in Figure 1.2. When the distribution plotted on the log scale has the shape of a Gaussian (normal) distribution, we refer to it as a log normal distribution, which is quite a common form for particle size distributions.

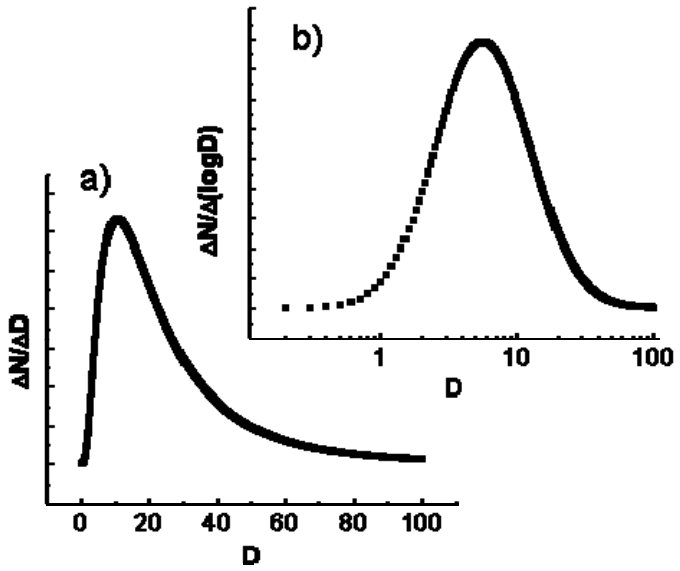

Figure 1.2: Comparison of a log normal distribution plotted as a function of the particle diameter and as a function of the log of the diameter. A log normal distribution appears as Gaussian distribution when plotted on the log scale.

Returning now to Figure 1.1, it is evident that on the basis of number concentration, the small or ultrafine particles dominate. In terms of mass or volume, Figure 1.1c shows that the fine and large particles dominate. Figure 1.1b shows the surface area distribution, in which the fine particles dominate. These three particle size ranges affect human health and the environment in different ways. For instance, the ultrafine particles can be particularly

damaging to the lungs because they are easily inhaled into the deepest parts of the lungs, whereas the large particles are generally stopped in the nasal passages. Because of their large surface area, the fine particles might be expected to dominate gas-surface reactions in the troposphere. Finally, because light scattering is strongly affected by particle size, the particles' effect on visibility and on the reflection of solar light is also strongly affected by particle size.[9]

The approach to mass spectrometric detection of these particles is dictated by the particle size and mass distribution. When single particle analysis is no longer feasible as a result of their small size, an approach that studies the mass spectrum of an ensemble of particles is still possible, albeit at the expense of single particle information. Most instruments are designed for specific particle size ranges because the ionization scheme as well as data collection approach for single particle and ensemble particle analysis are quite different.

The second challenge in aerosol mass spectrometry is associated with the mixture of various compounds. Salts are not readily vaporized, and in the early stages of vaporization when the density is high, tend to recombine with oppositely charged ions, thereby making quantization difficult, if not impossible. Organic species include semi-volatile molecules that vaporize as the particle is transported into the vacuum system, before reaching the ionization region. At the other extreme, high mass oligomers are difficult to vaporize and thus may be underestimated. Finally, fragile organics, often combined with oligomers, fragment extensively when vaporized and ionized.

Crustal matter such as dust provides other challenges. Due to the settling tendency of coarse mode crustal particles, early studies examined bulk soil samples, making source

apportionment difficult. More recent studies are able to suspend dust particles and examine them in a single particle manner.[10]

Because different molecular species require different methods of vaporization and ionization, it is readily apparent that no single instrument can provide all of the desired information. Several different instrumental configurations exist, each having its own particular advantage for the intended application. The basic principles underlying instrument design and performance also have "spin-off" applications beyond mass spectrometry.

The Aerosol Mass spectrometer

A generic diagram of an aerosol mass spectrometer is shown in Figure 1.3. The important components are 1) one or more optional aerosol conditioning devices upstream of the mass spectrometer, 2) a particle inlet and differential pumping system where particle sizing is usually performed, 3) a source region where particle vaporization and ionization occurs, and 4) a mass analyzer.

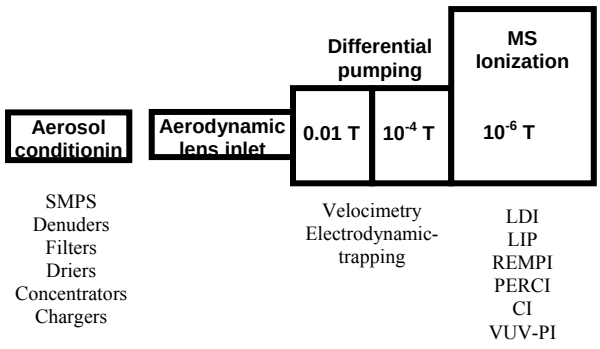

Figure 1.3: Block diagram of an aerosol mass spectrometer, the particle inlet and three chambers evacuated by three pumps, P_i. P_1 can be either a mechanical pump or a turbomolecular pump. Typical operating pressures (in Torr) are shown.

Essentially all instruments use an aerodynamic lens (to be described) to bring fine and large particles suspended in air into the vacuum system and to direct the particles efficiently toward the ionization region. Because the aerodynamic lens design is particle size dependent, the mass spectrometer must be optimized for specific size ranges already at this early stage of sample introduction. The aerosol sizing approach also depends on the size range of interest and as such is handled differently in different instruments. A final major diversity among various instruments lies in the vaporization/ablation/ionization systems in that some instruments use a single laser to accomplish all three functions, whereas others separate the vaporization and ionization steps. The ionization methods include electron impact, multiphoton ionization, vacuum UV photoionization, electron capture, and chemical ionization. Mass analysis is accomplished primarily by time of flight (TOF), quadrupole mass filters, or quadrupole ion traps.

Aerosol particle inlets

Aerosols are suspended in air by Brownian motion, and are introduced into the mass spectrometer through a 100-200 μm nozzle. The nozzle size is limited by a number of factors, the major one being the pumping speed available for portable instruments. The gas flow through a 100 μm orifice from atmosphere into a vacuum is 0.1 L-atm/min (1.7 cc-atm/sec). A pump with a conductance of 200 L/sec can thus maintain a pressure of 6×10^{-3} Torr in the first region of the differential pumping system.

The number of particles entering through this inlet nozzle can be determined from the particle number density. Thus a particle density of 10^3 particles/cm^3 would result in the introduction of 1,700 particles/sec into the inlet system. If only the total particulate mass is

of interest, we need to consider the mass density, which can range from 1 to 100 μg/m^3, the former corresponding to very clean air.[8] A typical density of 30 μg/m^3 will inject about $3x10^{-11}$ g sec^{-1} or 30 pg/sec of material into the MS.

Aerodynamic lens inlet for particles from 30-5000 nm: A critical component to aerosol mass spectrometers is the sample introduction system. The introduction of just 30 pg/sec of material is sufficiently small to require a very efficient particle transport system from the 100 μm orifice to the ionization region. Ten years ago, McMurry and co-workers developed an aerosol inlet, a so-called aerodynamic lens, which consists of a 100 μm flow limiting orifice attached to a 1 cm inner diameter, 30 cm long tube.[11,12] A series of carefully designed and machined apertures gently force the particles to the center of the tube by the time they reach the end of the lens where a 2 mm nozzle accelerates the particles into the vacuum (Figure 1.3). The apertures can be designed to pass only particles of a particular size, or a range of sizes, and a recent article from the McMurry group provides prescriptions and a program for a lens design for specific particle size ranges.[13,14,15] The particles inside the aerodynamic lens, where the pressure is approximately 2 Torr, are still suspended by Brownian motion and thus travel at the average gas flow speed of about 8 m/sec. However, as they pass through the 2 mm expansion nozzle into a pressure of .01 Torr, they are accelerated by numerous gas-particle collisions to a final speed of between 50 and 200 m/s. Because the lens focuses the particles into the middle of the exit nozzle, and because of the statistically very large number of collisions, the net force exerted on the particle is very much forward directed so that the particle beam exiting the nozzle has a very low divergence, which is ideal for transporting the particle to the ionization region. It has been estimated that the 90% of the particles with a diameter of 500 nm that enter the 100 μm nozzle are

transported to the center of the ionization region.[16] However, the divergence of the particle beam increases dramatically as the particles become smaller and is the major reason for decreasing transmission of particles below 100 nm.[17] Zelenyuk and Imre[18] recently optimized their system, which permits them to detect particles down to 50 nm. Johnston and co-workers found that they could focus charged particles < 50 nm in diameter using an electrostatic field [19] and <10 nm in diameter using an electrodynamic field.[20] A forthcoming article by Johnston and coworkers describes a system for electrodynamic focusing and trapping of particles below 30 nm. Also, a new study by McMurry and coworkers details an aerodynamic lens that can pass particles 3 – 30 nm in diameter with 50 – 80% efficiency respectively. This is particularly important in that it helps to bridge the gap between particles less than 3 nm in diameter which can only be focused using electrodynamic lenses, and particles tens of nanometers and larger which cannot be focused with electrodynamics due to the high required voltages.

1.2 Particle Sizing

The geometric diameter of an aerosol particle can be determined from an SEM image. However, on-line determinations that depend on indirect methods such as light scattering, diffusion, or sedimentation rates, are sensitive to both the geometric or physical diameter, D, as well as the particle's density, ρ. The relationship among the various definitions of particle sizes for spherical as well as non-spherical particles has been reviewed and quantified by deCarlo *et al.*[21] For instance, a volume equivalent diameter, d_{ve}, can be defined for non-spherical particles such that $d_{ve} = (6V/\pi)^{1/3}$, where V is the physical volume of the particle

Particle sizing outside the mass spectrometer can be accomplished by various methods depending on particle size. Particles with diameters in excess of 3 nm can be size selected by differential mobility analyzers (DMA) in which particles suspended in air by Brownian motion, are electrically charged and pass through an inhomogeneous electrical field, much like a cylindrical mirror electrostatic analyzer. In the DMA the collisional drag force is balanced against the electric field force, which makes this measurement for spherical particles proportional to the physical diameter, D. Such DMA's can be placed in front of the MS inlet nozzle to pre-select the particle size.

A scanning mobility particle sizer (SMPS, TSI Inc., Shoreview, MN) combines a DMA and a condensation particle counter (CPC). The SMPS can operate in one of two different modes. First, by scanning the voltage placed on the rod in the DMA, one can scan over the entire range of particle sizes. As particles pass through the DMA they are sent to the CPC, where their concentration and size distribution are determined. This is helpful for field studies, allowing particle composition and size to be correlated. Additionally, the DMA can be set to pass one given particle size only, to permit the study of monodisperse particles.

Two kinds of aerodynamic diameters are commonly used. When a particle is allowed to drift vertically through a gas by the earth's gravitational force, its terminal velocity will be related to its aerodynamic diameter, d_a, which for spherical particles is equal to $D(\rho/\rho_o)^{1/2}$, where the ρ's are the particle density and standard density of 1 g/cc, respectively. Particles with diameters in excess of 30 nm can also be size selected in the mass spectrometer by measuring their terminal velocity with which they exit the aerodynamic lens. This vacuum aerodynamic diameter, d_{va}, differs from the d_a because the particles are accelerated from a pressure of 1-2 Torr in the aerodynamic lens into the first stage of the differential pumping

region, which has a pressure of about 10^{-2} Torr. The latter is in the molecular flow regime in which collisions between particles and gas are essentially stopped. The result is that the vacuum aerodynamic diameter for spherical particles is given by $d_{va} = D(\rho/\rho_o)$.

The terminal velocities of the aerosol particles exiting the aerodynamic lens have been fitted to the empirical equation (1.1) proposed by Jayne *et al*.[22]:

$$v = \frac{v_g}{1 + \left(d_{va}/d^*\right)^b} \tag{1.1}$$

where d_{va} is again the vacuum aerodynamic diameter, v is the particle velocity, v_g is the molecular velocity of the jet expansion, and d^* and b are fitted coefficients. d^* represents the characteristic diameter for particle expansion from the aerodynamic lens. In the Jayne study, $d^* = 27.2 \pm 0.5$ nm, and $b = 0.479 \pm .004$. The velocity of the gas, v_g, can be obtained from the expansion enthalpy of 5/2RT and the molecular weight of the gas, which for air at 298 K yields about 600 m/s. A plot of v versus the aerodynamic diameter was created with particles of various densities, but plotted as function of their vacuum aerodynamic diameter, $D\rho$, discussed above. This variation of velocity with particle size continues down to quite small particles, but eventually, when the particles diminish in size to 1 nm, their final velocity approaches the terminal beam velocity of the gas and thus becomes independent of particle size.

The particle velocity can be measured in two ways. The Aerodyne MS instrument uses a chopper wheel that selects clumps of particles and uses the arrival of ions at the detector to determine the velocity and thereby the particle size.[22] Because the flight time of the particles from the chopper wheel to the ionization region is on the order of a millisecond, and the ion TOF in the mass analyzer is tens of μs, the ion transit time is

negligible compared to the particle flight time. This approach to velocity measurement is applicable to a very broad range of particle sizes, and is not necessarily limited to single particle analysis. In fact, its virtue lies in its ability to size large fluxes of small particles, for which single particle MS is in any case not possible. The major shortcoming is the small duty cycle of the chopper wheel. The chopper wheel is 5 cm in diameter and has two 0.13 cm slits oriented 180° apart, leading to a 1.8% duty cycle.

The other in-situ method for particle velocity determination is based on measuring the transit time of particles as they pass through two continuous laser beams that are separated by approximately 10 cm. The light scattered by the single particles as they pass through the beam is monitored by photomultipliers. Green diode lasers at 532 nm are preferred over the red HeNe lasers (632.8 nm) because they scatter light more efficiently and their light is detected with greater sensitivity by the photomultipliers. This method is applicable to small fluxes of larger particles for which single particle MS is possible.

The light scattering is strongly dependent on particle size, the wavelength of the light, as well as the scattering angle. In the Rayleigh limit, where the particles are much smaller than the wavelength of the light, the scattering intensity is proportional to D^6, where D is the particle diameter. This strong dependence of the scattering intensity on the particle diameter means that light scattering is limited to particles with a diameter greater than about 100 nm. However, light scattering has recently been reported for smaller particles using low wavelength light generated by synchrotron radiation.[23] Because of the diminished scattering intensity of small particles, recent innovations that maximize the collected light include the use of elliptical mirrors that collect the full 4π solid angle of scattered

light.[17,18] One focal point is the intersection of the particle and laser beams, and the PMT is placed at the other focal point.

Although the scattering intensity varies rather smoothly with scattering angle for small particles,[24] the functional form becomes more complicated with large particles because the light is internally reflected in the particle. Figure 1.4 shows scattering intensity versus scattering angle for three different sized particles as represented by the size parameter α, where:

$$\alpha = \frac{\pi d_p}{\lambda} \tag{1.7}$$

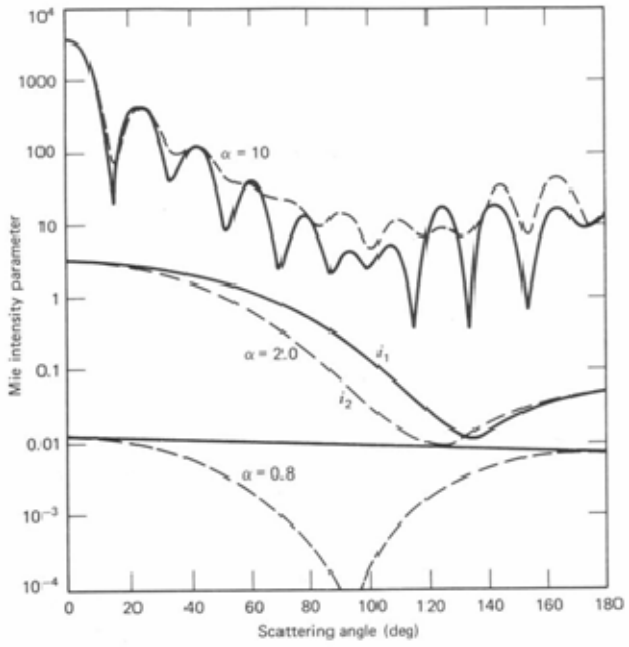

Figure 1.4: Light scattering as a function of angle for various values of α taken with permission from Hinds. [73] For a photon wavelength of 532 nm, the three value of α (10, 2, 0.8) correspond to particle diameters of 1.7 μm, 338 nm, and 135 nm, respectively.

These interference effects, which can be modeled with Mie theory,[24] yield an intensity pattern that varies strongly with the scattering angle. Such angular distributions have been used to determine very precise diameters for spherical particles.[25,26,27] However, the measurement of angular distributions is complicated and does not lend itself for use in mass spectrometric analysis of particles. In addition, the scattering is much more complex for non-spherical particles. The more easily accomplished alternative, to measure the light intensity at a single angle, is not reliable, as shown by Salt *et al.* [28]

1.3 Ionization Methods

The method of ionization employed in aerosol MS must be matched to the types of aerosol particles. Ten to twenty Hz pulsed lasers can be used to ablate/ionize large particles (0.3 – 5 μm) that enter the MS at rates less than 20 times per second. They require that the laser be pulsed at random times when the light scattering station indicates the arrival of a particle in the ionization region. Electronic units to manage the pulsing requirements for various lasers, in particular Nd:YAG lasers whose flash lamps must be pulsed some 200 μs prior to the laser pulse, have been described.[29,30] Although such low frequency pulsed lasers would not be efficient in ionizing the smaller particles that enter the MS at the rate of 1000 per second or more, the use of a 1 kHz excimer laser would appear to be an attractive option. However, the latter has not been reported in aerosol MS work. In general, a more efficient approach for quasi-continuous arrival times of small particles is the use of a continuous ionization method such as electron impact or chemical ionization.

The chemical composition of the particle also plays a role in the choice of ionization methods. Salts, metals, and crustal particles are most efficiently ablated and ionized by a

strong UV laser pulse, whereas the more easily vaporized organic molecules are better ionized by electron impact, chemical ionization, electron attachment, or one-photon vacuum UV ionization.

1.3.1 Pulsed laser ionization methods

1.3.1.1 Laser desorption/ionization (LDI)

Johnston and Murphy were among the first to couple laser desorption/ionization (LDI) with time-of-flight mass spectrometry in the early 1990s.[31,32] Particles were detected by monitoring light scattering signal from a single HeNe laser passing through the ionization region, similar to the methods developed by Sinha.[33] The photomultiplier signal triggered an excimer laser (193 nm) that desorbed and ionized the single aerosol particles. The single HeNe light scattering station located in the ionization region, did not permit sizing of the particles, but rather was used simply to signal the arrival of a particle in the ionization region. This arrangement is possible with excimer and nitrogen lasers that can be triggered within a few hundred nanoseconds, during which time particles move less than 100 μm.

The LDI method is extremely sensitive because a very large number of photons (ca 10^{16} per pulse) can be directed at a particle that is known to be in the ionization region. In principle, every laser shot should generate larges fluxes of ions. Single particles with diameters as small as 50 nm have been detected with good signal to noise.[18,34]

In 1994, Prather *et al.*[30] used LDI with the fourth harmonic of a Nd:YAG laser at 266 nm. As mentioned above, the flash lamps of this laser must be triggered about 250 μs prior to firing the Q-switch (which triggers the laser light pulse) so that the light scattering station must be located approximately 10 cm from the ionization region. In other words, the

laser must be triggered well before the particle reaches the ionization region. The addition of a reflectron improved mass resolution and also resulted in a more compact ion TOF, which is especially useful in portable instruments.[35]

The UV laser desorption/ionization approach is ideal for particle sizes in excess of 200 nm and for measuring salt and metal containing particles, which are indeed difficult to ionize by other methods. It is less useful for organic species because of the considerable fragmentation induced. This is a result of the high laser intensity required to ablate and ionize the particle. Any organic ions generated will readily absorb multiple UV photons resulting in massive fragmentation. However, certain mass fragments, such as 37, 39, and 41 are useful markers for the presence of organic species with different functionalities in the particles.[36] Aromatic hydrocarbons are a major exception in that they often yield significant parent ion signal because they tend to be rather stable ions and because they are readily ionized by a resonant 1+1 laser absorption scheme.[37] It is possible to manipulate the desorption /ionization process to enhance the formation of molecular ions. For example, use of a lower pulse energy laser beam to decrease the amount of fragmentation would be beneficial. Also, Reilly and coworkers employ a system to coat particles entering the mass spectrometer with a matrix that promotes large ion formation by matrix-assisted laser desorption ionization.

One of the problems in quantitative determinations of salt and metal containing particles by laser desorption/ionization is matrix effects.[38,39] The high concentration of positive and negative ions generated by the laser pulse impinging on a 1 μm particle, leads to ion-ion recombination reactions that deplete the signal. Indeed, Dessiaterik *et al.*[40] demonstrated that for low ion concentrations of RbCl in a solution of ethylene glycol, the

observed ion signal is linear with the concentration, whereas it levels off at concentrations in excess of 10^{-4} M, and becomes completely insensitive to the ion concentration above 10^{-3} M. Although absolute quantitation under these circumstances is clearly not possible, relative yields among similar particles are still useful.

1.3.1.2 Two-Step Desorption and Ionization

Gas-phase ionization methods can be used for aerosol analysis if they are coupled with a separate thermal or laser desorption step. Several configurations are described below.

Resonance Enhanced Multi-photon Ionization (REMPI)

Multiphoton ionization can occur by a non-resonant simultaneous absorption of several photons. The greater the number of photons involved, the more tightly the laser must be focused in order to drive the transition. The cross section is approximately related to I^n, where I is the laser intensity and n the number of photons absorbed in the non-resonant step. If the molecule has a real electronic state at an energy that is a multiple of the photon energy, the cross section increases significantly, and is termed resonance enhanced multiphoton ionization, or REMPI. In general, REMPI is not a very useful approach for aerosol mass spectrometry because, a) the particle beam can easily be missed by the tightly focused laser beam, and b) the ion signal intensity can vary by orders of magnitude from one molecule to another. The one exception is a 1:1 two-photon absorption in which the laser does not have to be focused because the absorption does not involve any non-resonant steps so that the process becomes linear. That is, the ion signal intensity obtained by 1:1 photoionization of a diffuse sample is independent of the laser focal volume. This ionization method is applicable primarily to aromatic molecules because the benzene ring has a strong absorption around 266

nm (4.66 eV), which lies more than half way to the ionization limit of aromatic molecules (generally about 9 eV).

Vacuum UV (VUV) ionization

In order to overcome the limitations of UV laser desorption/ionization for speciating the organic fraction of aerosol particles, Baer and Miller introduced vacuum UV photoionization in conjunction with a prior vaporization step.[41] An IR laser, (CO_2 at 10.2 μm or a tunable OPO in the 3 μm region) was used to gently vaporize the particles consisting of organic species. The VUV laser, triggered several μs later, ionized a low density plume of gas phase species, which eliminated the matrix effects caused by ion molecule reactions in high density samples. The fragmentation is reduced because the high intensity UV laser is replaced with a low intensity VUV laser pulse, which can ionize the sample gas with single photon absorption, thereby eliminating multi-photon processes. This approach is limited to particles above about 300 nm since the particle mass must be above the detection limit. Johnston and co-workers extended the VUV ionization method to particles of arbitrary size by collecting the particles on a cold finger. After a sufficient number of particles are deposited, the sample is flash vaporized with an IR laser, followed by photoionization with the VUV laser pulse.[42]

Coherent VUV radiation can be generated by two methods. A particularly convenient method is 3rd harmonic generation using the 355 nm Nd:YAG laser pulse directed into a cell containing about 14 Torr of Xe diluted with 165 Torr of Ar for phase matching purposes.[43] Three 355 nm photons directed into the sample are converted into one 118 nm photon (10.5 eV) out by a coherent process that requires a focused Nd:YAG laser with about 10-20 mJ of pulse energy. This process, which has an efficiency of about 10^{-7}, generates approximately

10^{10} VUV photons per pulse.[44] Given a typical absorption cross section of 10^{-18} cm^2, it is evident that only about 1 in 10^7 molecules will be ionized. This limits the VUV laser approach to particle diameters greater than about 300 nm. In general, the detection limit for VUV photoionization of a given molecule is on the order of 100 ng/m^3, which does not make it a very competitive method for detecting real tropospheric aerosols, whose mass density can be as low as 1 ng/m^3. However, it is very useful for laboratory studies where the particle densities can be raised.

A more general method for VUV photon generation is by two-color four wave mixing. [44,45] A convenient scheme involves the 2-photon excitation of the Kr $^2P_{3/2}$ state[46] with a pulse of $\lambda_1 = 212.5$ nm light and a simultaneous pulse of tunable visible light (λ_2). Sum and difference mixing results in the production of $\lambda_3^{-1} = \lambda_1^{-1} \pm \lambda_2^{-1}$. Although this approach is more complicated, requiring two laser photons that have to be carefully aligned, the output is a tunable and more intense because it involves only a non-resonant two photon process rather than a coherent three photon process as in third harmonic generation.

Although photoionization by VUV photons dramatically reduces ion fragmentation[45,47], it is not yet clear how effective VUV photoionization is for identifying molecular constituents in tropospheric particles. The 10.5 eV photoionization mass spectra of the α-pinene ozonolysis products reported by Tolocka and Johnston indicate that the reduction in fragmentation over electron impact is significant, but not sufficiently dramatic to permit the identification of more than a few of the reaction products.[48] A two-dimensional approach such as provided by thermal desorption MS[49] coupled with photoionization and high mass resolution MS will be needed to identify the many products in these particles.

1.3.1.3 Laser Induced Plasma

Originally demonstrated by Reents[50,7] and subsequently Zachariah[51,52], formation of a laser induced plasma is similar to LDI except that a much higher laser irradiance is used. Whereas a few millijoules of ultraviolet radiation are moderately focused in the mass spectrometer source region to perform LDI, formation of a laser induced plasma requires tight focusing of a >100 mJ pulse, typically from a Nd:YAG laser operating at 532 nm. Under these conditions, the "complete ionization limit" is thought be achieved, where the particle is assumed to be completely disintegrated to atoms and the atoms quantitatively converted to positively charged ions. The positive ion spectrum shows a series of singly and multiply charged ions for each element in the particle. The negative ion spectrum shows only electrons. An advantage of the complete ionization limit is that the combined signal intensities of the series of ions for each element give a semi-quantitative measure of atomic composition.

1.3.1.4 Pulsed Electron Capture Ionization

The capture of low energy electrons as a soft ionization method has been used by mass spectrometrists for many years.[53,54,36] Petrucci and co-workers have developed a photoelectron resonance capture ionization (PERCI) version for use in aerosol mass spectrometry[55,56]. Although electron capture ionization is not by its nature a pulsed method, Petrucci employs a 10Hz, tunable (235-300nm) UV laser focused onto the surface of an aluminum photocathode to generate low-energy and more or less mono-energetic electrons in a pulsed manner. Given the work function of the Al metal, the photoelectrons are generated in a range of energies from 0.05-1.20 eV, which is a convenient range for efficient electron capture ionization.

The electron attachment process generally involves the loss of a hydrogen atom so that the resulting negative ion is closed shell, thereby imparting significant stability.

1.3.2 Continuous Ionization Methods

1.3.2.1 Electron Impact Ionization

Electron impact (EI) is a universal ionization method that has two important attributes. One of these is that a large body of standard spectra collected with 70 eV electrons is available in the literature. This permits the establishment of search routines that can readily identify a compound based on its mass spectrum. For this purpose, it is essential that the MS for a molecule consists of multiple fragment ion peaks that provide a fingerprint for that molecule. The other virtue is that the total integrated intensity of the spectrum for a given molecule is proportional to its pressure in the ionization source. That is, the peak intensities can be quantitatively related to the molecule's concentration. The total intensity is approximately proportional to the total number of electrons in the molecule. This property is not shared with photoionization at a given photon energy because of numerous resonances throughout the molecule's photoabsorption spectrum.

EI has been adopted by the Aerodyne AMS instrument because of the above features. However, tropospheric particles often contain a bewildering number of molecules that cannot be distinguished by an EI spectrum because of the numerous fragment ion peaks. Nonetheless, basic information about organic composition can be extracted. More detailed molecular information requires multi-dimensional approaches. Although such information can be obtained in the laboratory by methods such as GC/MS or LC/MS that separate the molecules prior to introduction into the mass spectrometer, no "real-time" aerosol mass spectrometer has managed to achieve this. One step in that direction was pioneered by

Ziemann and co-workers, who collect the particles on a cold finger. Subsequent programmed thermal desorption releases the molecules from the probe in order of their decreasing volatility, thereby providing a crude pre-separation of the sample prior to ionization and mass analysis.[57,58] An example of some thermal desorption data is shown in Figure 1.5.

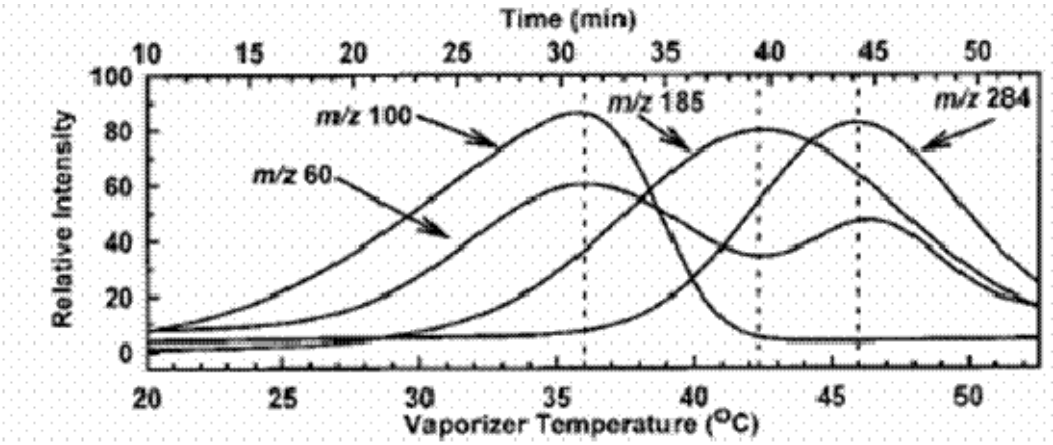

Figure 1.5: Thermal desorption mass yields of particles created by ozonolysis of 1-tetradecene. The double humped shape for m/z 60 shows that this ion comes from both a low-volatile as well as a more highly volatile reaction product. Taken with permission from Tobias and Ziemann .[49]

1.3.2.2 Continuous Vacuum UV photoionization

Synchrotron radiation, which produces a flux of vacuum UV photons in excess of 10^{15} photons/sec, has recently been used to photoionize molecules from aerosol particles vaporized by a resistively heated filament.[47] The photon beam generated by the undulator is extremely collimated, and can be focused by grazing incidence mirrors to a spot size of 100 x 200 μm, which is an ideal source for time of flight analysis. Synchrotron light also has the advantage of easy tunability, so that the photon energy can be chosen to minimize the ion

fragmentation. The major disadvantage of this source is that the experiment must be transported to the synchrotron, and is therefore limited to laboratory based experiments.

1.3.2.3 Chemical Ionization

Chemical ionization (CI) is a sensitive and gentle method of ion formation that generally produces only a single mass ion. A very useful reaction is proton transfer, which generates the M+1 ion. Common reagents used for proton transfer include protonated water clusters, $H^+(H_2O)_2$, and protonated methanol clusters, $H^+(CH_3OH)_2$. The major difference between EI and PI on the one hand, and CI on the other, is that the latter produces closed shell ions, whereas the standard ionization processes generate open shell radical cations that are often unstable. Because many of the molecules found in tropospheric aerosols are quite fragile, soft CI would appear to be an ideal choice for instruments designed to detect the organic fraction of the aerosol particles.[59,60] The sensitivity for oleic acid detection is on the order of ~ 200 ng/m^3 which corresponds to ~ 4 x 10^8 molecules/cm^3 (~ 0.02 ppb) in gas-phase units. Because many organic particulates in the troposphere contain organic molecules at a concentration of 1 ng/m^3, it is not clear that CI will be competitive with EI for ambient measurements.

CI has also been used by Lazar et al.[61] in a pulsed mode by reacting K^+ ions, produced by a pulsed excimer laser, with the vaporized aerosol sample. Another CI based instrument (TDCIMS) developed by Smith and co-workers,[62,63,64] is designed to analyze particles down to 10 nm. Ambient aerosol particles are charged in a unipolar aerosol charger and drawn into the TDCIMS instrument. They are then collected by an electrostatic precipitator for 6 minutes, desorbed by resistively heating the collection wire, and finally ionized via chemical ionization.

1.4 Mass Spectrometry

1.4.1 Mass Analyzers

The three major methods of mass analysis in aerosol mass spectrometers have been time of flight (TOF) and RETOF, quadrupole mass filter, and the quadrupole ion trap. The two major commercial instruments use an ion RETOF (TSI) and a quadrupole (Aerodyne). Of these, only the TOF can be used as a true single particle mass spectrometer. However, as shown by Reilly *et al.*, when the ion trap is operated in the mass selective instability mode, the RF voltage on the ring electrode is ramped, ejecting ions sequentially so that all of the ions can be detected.

The ion trap can also be used for MS/MS studies.[65] In principle, MS/MS provides information about the structure of a targeted mass peak in the mass spectrum, and thus could lead to the identification of a compound in the aerosol particle. On the other hand, difficulties in real-time data-dependent selection of precursor ions for MS/MS analysis and the need for manual interpretation of complex product ion spectra may inhibit its use in the field.

Because of the large number of molecular organic constituents in tropospheric particles, any given nominal mass peak most likely consists of several compounds. For instance, the m/z 98 peak can be attributed to C_7H_{14}, $C_6H_{10}O$, $C_5H_6O_2$, or $C_4H_2O_3$. These can be readily resolved by high resolution MS. Because the oxygen content of the peaks provide important information about the aerosol origin and its secondary reactions in the troposphere, this information is highly valuable. In the laboratory, several options for high resolution MS are available. Fewer options exist for field measurements. The installation of an orthogonal

RETOF mass analyzer may provide sufficient resolution to obtain such information for relatively low m/z ions, for example $C_3H_7^+$ and $C_2H_3O^+$ at a nominal m/z of 43.[66]

1.4.2 Portable Instruments

A major thrust in aerosol mass spectrometry has been the development of field portable instruments. Several EPA supersites have invited researchers with a variety of instruments in one location in order to collect atmospheric data for up to two years.[67] The types of measurements conducted have included data on wind direction and velocity, pollutant levels (ozone, CO, CO_2, NO_x, etc), relative humidity, and particulate matter. In the 1999 Atlanta supersite study, four aerosol mass spectrometers were operated simultaneously, and a study comparing the results was published.[67] The instruments in question were NOAA's Particle Analysis by Laser Mass Spectrometer (PALMS), University of California at Riverside's Aerosol Time-of-Flight Mass Spectrometer (ATOFMS)[68], University of Delaware's Rapid Single-Particle Mass Spectrometer (RSMS), and Aerodyne's Aerosol Mass Spectrometer (AMS). These instruments differed in their ionization methods (laser desorption/ionization for the PALMS, ATOFMS, and RSMS, and thermal vaporization followed by electron impact ionization for the AMS). Some were limited to particles with diameters in excess of 200 nm, while the AMS and RSMS could detect particles down to 15 nm. The AMS is optimized to detect and classify organic material, whereas the laser desorption/ionization instruments are best for refractory material such as soot, sodium chloride, and dust. This comparison demonstrates the need for various types of instruments in order to obtain a complete picture of the aerosol chemical content.

One of the earliest portable instruments, developed by Murphy and co-workers,[69,70] is designed to fit into the nose cone of an airplane, and can thus be used to monitor aerosol concentration and composition as a function of altitude and in the wake of aircraft or rockets.

1.4.3 Data handling

One of the problems in the deployment of field portable instruments is the volume of data collected. If an instrument collects single particle mass spectra at the rate of 3 per second for a period of 1 month, the number of stored spectra is close to 8 million. This provides a challenge for data storage, especially in the case of high resolution data. But an even greater problem involves data analysis. How can so much information be digested, and retrieved? A number of workers have devoted considerable effort in the area of chemometrics[71,72] to help resolve this issue.

1.5 Conclusion

The field of aerosol mass spectrometry continues to develop. This chapter has discussed several approaches that allow for the detection and speciation of a wide range of particle sizes and compositions. However, much work remains in order to continue to expand the range of size and types of particles that any one instrument can analyze. Finally, the continued advancement of portable instruments has also been extremely important to the aerosol mass spectrometry field. Portable instruments have been integral in source apportionment studies as well in studies which aim to examine real time effects of changes in meteorological conditions on particle size and composition. Despite all of these advancements, real atmospheric particles are too complex for one instrument to optimally

detect and quantify the composition of them all. Therefore, there is much room and need for the continued development of several different types of instruments.

References

[1] D. T. Seuss, K. A. Prather, Chem.Rev. 99 (1999) 3007.

[2] A. L. Hunt, G. A. Petrucci, Trends Anal.Chem. 21 (2002) 74.

[3] M. V. Johnston, J.Mass Spectrom. 35 (2000) 585.

[4] C. A. Noble, K. A. Prather, Mass Spectrom.Rev. 19 (2000) 248.

[5] D. M. Murphy, Science 307 (2005) 1888.

[6] D. M. Murphy, Mass Spectrom.Rev. in press

[7] W. D. Reents, Z. Ge, Aerosol Sci.Technol. 33 (2000) 122.

[8] B. J. Finlayson-Pitts, J. N. Pitts, Chemistry of the Upper and Lower Atmosphere: Theory, Experiments and Applications, Academic Press, New York, NY, 2000.

[9] H. C. Van de Hulst, Light Scattering by Small Particles, Wiley, New York, NY, 1957.

[10] P. J. Silva, R. A. Carlin, K. A. Prather, Atmos.Environ. 34 (2000) 1811.

[11] P. Liu, P. J. Ziemann, D. B. Kittelson, P. H. McMurry, Aerosol Sci.Technol. 22 (1995) 293.

[12] P. Liu, P. J. Ziemann, D. B. Kittelson, P. H. McMurry, Aerosol Sci.Technol. 22 (1995) 314.

[13] X. Wang, F. E. Kruis, P. H. McMurry, Aerosol Sci.Technol. 39 (2005) 611.

[14] X. Wang, A. Gidwani, S. L. Girshick, P. H. McMurry, Aerosol Sci.Technol. 39 (2005) 624.

[15] X. Wang, P. H. McMurry, Aerosol Sci.Technol. 40 (2006) 320.

[16] G. A. Petrucci, P. B. Fransworth, P. Cavelli, N. Omenetto, Aerosol Sci.Technol. 33 (2000) 105.

[17] Y. Su, M. F. Sipin, H. Furutani, K. A. Prather, Anal.Chem. 76 (2004) 712.

[18] A. Zelenyuk, D. Imre, Aerosol Sci.Technol. 39 (2005) 554.

[19] D. B. Kane, B. Oktem, M. V. Johnston, Aerosol Sci.Technol. 35 (2001) 990.

[20] S. Wang, C. A. Zordan, M. V. Johnston, Anal.Chem. 78 (2006) 1750.

[21] P. F. DeCarlo, J. G. Slowik, D. R. Worsnop, P. Davidovits, J. L. Jimenez, Aerosol Sci.Technol. 38 (2004) 1185.

[22] J. T. Jayne, D. C. Leard, X. Zhang, P. Davidovits, K. A. Smith, C. E. Kolb, D. R. Worsnop, Aerosol Sci.Technol. 33 (2000) 49.

[23] K. R. Wilson, A. N. Arrowsmith, M. Ahmed, S. R. Leone, Nano Letters 5 (2005) 1009.

[24] C. F. Bohren, D. R. Huffman, Absorption and Scattering of Light by Small Particles, Wiley, New York, NY, 1983.

[25] A. K. Ray, A. Souyri, E. J. Davis, T. M. Allen, Appl.Opt. 30 (1991) 3974.

[26] K. Chamaillard, C. Kleefeld, S. G. Jennings, D. Ceburnis, C. D. O'Dowd, J.Quant.Spectry.Radiative Transfer 101 (2006) 498.

[27] Y. Pavlyukh, W. Hubner, Phys.Rev.B 70 (2004) 245434-1.

[28] K. Salt, C. A. Noble, K. A. Prather, Anal.Chem. 68 (1996) 230.

[29] E. R. Mysak, Y. N. Dessiaterik, C. J. McKinney, R. E. Miller, T. Baer, Rev.Sci.Instrum. 77 (2006) 013301.

[30] K. A. Prather, T. Nordmeyer, K. Salt, Anal.Chem. 66 (1994) 1403.

[31] B. A. Mansoori, M. V. Johnston, A. S. Wexler, Anal.Chem. 66 (1994) 3681.

[32] P. J. McKeown, M. V. Johnston, D. M. Murphy, Anal.Chem. 63 (1991) 2069.

[33] M. P. Sinha, Rev.Sci.Instrum. 55 (1984) 886.

[34] D. A. Lake, M. P. Tolocka, M. V. Johnston, A. S. Wexler, Environ.Sci.Technol. 37 (2003) 3268.

[35] E. Gard, J. E. Mayer, B. D. Morrical, T. Dienes, D. P. Fergenson, K. A. Prather, Anal.Chem. 69 (1997) 4083.

[36] F. W. McLafferty, F. Turecek, Interpretation of Mass Spectra, University Science Books, Sausalito, CA, 1993.

[37] P. J. Silva, K. A. Prather, Anal.Chem. 72 (2000) 3553.

[38] D. S. Gross, M. E. Galli, P. J. Silva, K. A. Prather, Anal.Chem. 72 (2000) 416.

[39] D. B. Kane, M. V. Johnston, Environ.Sci.Technol. 34 (2000) 4887.

[40] Y. Dessiaterik, T. G. Nguyen, R. E. Miller, T. Baer, J.Phys.Chem.A 107 (2003) 11249.

[41] E. Woods III, G. D. Smith, Y. Dessiaterik, T. Baer, R. E. Miller, Anal.Chem. 73 (2001) 2317.

[42] B. Oktem, M. P. Tolocka, M. V. Johnston, Anal.Chem. 76 (2004) 253.

[43] S. E. van Bramer, M. V. Johnston, Appl.Spectrosc. 46 (1991) 255.

[44] J. W. Hepburn, in: A.B. Myers, T.R. Rizzo (Eds.), Laser Techniques in Chemistry, John Wiley and Sons Inc., New York, NY, 1995, p. 149.

[45] D. G. Nash, X. F. Liu, E. R. Mysak, T. Baer, Int.J.Mass Spectrom. 241 (2005) 89.

[46] J. Sugar, A. Musgrove, J.Phys.Chem.Ref.Data 20 (1991) 859.

[47] E. R. Mysak, K. R. Wilson, M. Jimenez-Cruz, M. Ahmed, T. Baer, Anal.Chem. 77 (2005) 5953.

[48] M. P. Tolocka, K. J. Heaton, M. A. Dreyfus, S. Wang, C. A. Zordan, T. D. Saul, M. V. Johnston, Environ.Sci.Technol. 40 (2006) 1843.

[49] H. J. Tobias, P. J. Ziemann, Environ.Sci.Technol. 34 (2000) 2105.

[50] W. D. Reents, M. Schabel, Anal.Chem. 73 (2001) 5403.

[51] R. Mahadevan, D. Lee, H. Sakurai, M. R. Zachariah, J.Phys.Chem.A 106 (2002) 11083.

[52] D. Lee, K. Park, M. R. Zachariah, Aerosol Sci.Technol. 39 (2005) 162.

[53] A. Cappiello, G. Famiglini, A. Lombardozzi, A. Massari, G. G. Vadalia, Journal of the American Society for Mass Spectrometry 7 (1996) 753.

[54] H. J. Leis, G. Fauler, G. N. Rechberger, W. Windischhofer, Current Medicinal Chemistry 11 (2004) 1585.

[55] B. W. LaFranchi, G. A. Petrucci, J.Am.Soc.Mass Spectrom. 15 (2004) 424.

[56] B. W. LaFranchi, J. Zahardis, G. A. Petrucci, Rapid Comm.Mass.Spectr. 18 (2004) 2517.

[57] H. J. Tobias, P. J. Ziemann, Anal.Chem. 71 (1999) 3428.

[58] H. J. Tobias, P. M. Kooiman, K.S. Docherty, P. J. Ziemann, Aerosol Sci.Technol. 33 (2000) 170.

[59] J. D. Hearn, G. D. Smith, J.Phys.Chem.A 108 (2004) 10019.

[60] J. D. Hearn, G. D. Smith, Anal.Chem. 76 (2004) 2820.

[61] A. C. Lazar, P. T. A. Reilly, W. B. Whitten, J. M. Ramsey, Anal.Chem. 72 (2000) 2142.

[62] D. Voisin, J. N. Smith, H. Sakurai, P. H. McMurry, F. L. Eisele, Aerosol Sci.Technol. 37 (2003) 417.

[63] J. N. Smith, K. F. Moore, P. H. McMurry, F. L. Eisele, Aerosol Sci.Technol. 32 (2004) 100.

[64] J. N. Smith, K. F. Moore, F. L. Eisele, D. Voisin, A. K. Ghimire, H. Sakurai, P. H. McMurry, J.Geophys.Res. 110 (2005) D22S03.

[65] P. T. A. Reilly, R. A. Gieray, W. B. Whitten, J. M. Ramsey, Environ.Sci.Technol. 32 (1998) 2672.

[66] F. Drewnick, S. S. Hings, P. F. DeCarlo, J. T. Jayne, M. Gonin, K. Fuhrer, S. Weimer, J. Jimenez, K. L. Demerjian, S. Borrmann, D. R. Worsnop, Aerosol Sci.Technol. 39 (2005) 637.

[67] A. M. Middlebrook, D. M. Murphy, S.-H. Lee, D. S. Thompson, K. A. Prather, R. J. Wenzel, D.-Y. Liu, D. J. Phares, K. P. Rhoads, A. S. Wexler, M. V. Johnston, J. L. Jimenez, J. T. Jayne, D. R. Worsnop, I. Yourshaw, J. H. Seinfeld, R. C. Flagan, J.Geophys.Res. 108 (2003) SOS 12/1.

[68] M. Jaoui, K. G. Sexton, R. M. Kamens, Atmos.Environ. 38 (2004) 2709.

[69] D. J. Cziczo, D. M. Murphy, D. S. Thomson, M. N. Ross, Geophys.Res.Lett. 29 (2002) 33/1.

[70] D. S. Thompson, M. E. Schein, D. M. Murphy, J.Aerosol Sci. 33 (2000) 153.

[71] D. P. Fergenson, D. Y. Liu, P. J. Silva, K. A. Prather, Chemom.Intell.Lab.Syst. 37 (1997) 197.

[72] D. J. Phares, K. P. Rhoads, A. S. Wexler, D. B. Kane, M. V. Johnston, Anal.Chem. 73 (2001) 2338.

[73] W. C. Hinds, Aerosol Technology: Properties, Behavior, and Measurement of Airborne Particles, Wiley Interscience, New York, NY, 1982.

CHAPTER 2

Aerosol Particle Mass Spectrometry with low Photon Energy laser Ionization

The problem of excessive ion fragmentation observed in the mass spectra of organic aerosols is addressed by varying the photon energy used to ionize the vaporized particles. Oleic acid aerosols are vaporized by either an IR CO_2 laser or by impaction on a heater and ionized by pulsed laser radiation produced by either 3rd harmonic generation in Xe (118 nm; 10.48 eV) or by resonance difference frequency mixing in Kr (142 nm; 8.75 eV). The use of the lower energy laser light greatly reduced the fragmentation of the oleic acid ions. However, spectra of oleic acid particles taken at several different CO_2 laser powers showed that the internal energy of molecules in the vapor plume vary in time so that the appearance of the mass spectrum is a function of the delay time between CO_2 and VUV laser pulses. Hot molecules produced in the early stages of vaporization generated large amounts of fragment ions, whereas the mass spectra of colder molecules consisted predominantly of parent ions. Vaporization with the heater on the other hand, shows a more uniform heating of the particle, with very little ion fragmentation. The ionization energy (8.6 ± 0.1 eV) and the fragment ion appearance energy (9.0 ± 0.1 eV) of oleic acid were determined by photoelectron photoion coincidence spectrometry.

2.1. Introduction

Mass spectrometric analysis of aerosol particle constituents has become an essential tool not only for laboratory studies of model aerosols [1-8] but also in field studies, where rapid detection and identification of aerosols is highly desirable.[9-16] Atmospheric aerosols contain a wide range of substances including inorganic salts, metals, dust, soot, and organic species.[17] The ideal analysis tool should be able to identify each molecule, and provide a quantitative measure of its concentration. Unfortunately, current instruments are far from achieving this goal. This paper deals with the analysis of organic species in aerosol particles. The difficult issue in their analysis is the ease with which they fragment upon ionization. If a particle contains a large range of organic molecules, the identification is clearly impeded by extensive fragmentation, which results in a broad range of ion peaks whose identity is then difficult to establish.

Current aerosol mass spectrometers use either continuous or pulsed ionization schemes. The former generally employs electron impact,[18,19] or chemical ionization.[20,21] The pulsed ionization approach depends on lasers that are fired whenever a particle appears in the ionization region. This has the advantage that the laser photons are efficiently used when an aerosol particle is in the ionization region. The pulsed laser approach is ideal for large particles (0.2 to 5 μm in diameter) because their arrival at the ionization region can be determined by light scattering from continuous lasers.[4,22,23] The continuous ionization scheme is clearly advantageous for the detection of a large number of small particles whose arrival time cannot be detected by laser light scattering, and whose arrival at the ionization region is in any case quasi-continuous.

Fragmentation of ions is a result of internal energy imparted to the ion during the vaporization or ionization process. Ionization by a pulsed UV laser, in which ionization is

achieved by multiphoton excitation, results in particularly high ion internal energies because, once formed, the ion continues to absorb photons during the 5 -10 ns photon pulse. It is not unusual to detect mostly C^+ ions and the observation of parent ion peaks is rare.[8] For this reason, a single laser ablation/ionization scheme does not work for organic species. In response to that, Worsnop *et al.*[19] have developed a two stage vaporization/ionization scheme in which the particles are directed at a heater located in the ionization region, where the vaporized molecules are ionized by electron impact. This provides excellent sensitivity and reduced fragmentation in comparison to the UV laser ablation/ionization scheme. However, ion fragmentation by electron impact of organic mixtures remains a difficult problem. Reducing the electron energy from 70 eV to lower energies would reduce fragmentation, but would also reduce the ionization efficiency.

Our approach to reducing ion fragmentation has been to use pulsed vacuum UV laser radiation,[4] which has now also been implemented by Oektem *et al.*[24] The aerosol particles are vaporized either by the absorption of infrared radiation from a pulsed CO_2 laser, or by impinging on a heater. Once vaporized, the molecules are ionized by 118 nm (10.48 eV) radiation generated by the frequency tripling of a 355 nm Nd:YAG laser pulse in a Xe/Ar mixture. This approach has dramatically reduced ion fragmentation because the 10.48 eV photon is close to the ionization energy of many molecules such as benzene, nitrobenzene, aniline, etc. However, we have found that as larger molecules with lower ionization energies are investigated, the 10.48 eV photon energy is too high and thus results in considerable ion fragmentation. This was a particular problem with the analysis of reaction products from the reaction between ozone and oleic acid aerosol particles.[25] The mass spectra of the reacted oleic acid particles vaporized by the CO_2 laser and ionized by the

10.48 eV VUV photons were characterized by a broad range of lower mass peaks that prevented identification of reaction products.[25] Thus, a softer ionization approach would be highly desirable.

As stated before, ion fragmentation is a result of high internal energy, which is caused both by heating of the neutral molecules with, for instance the CO_2 laser or the heating element, and by the VUV laser. Unfortunately, heating of the oleic acid cannot be avoided if sufficient material is to be vaporized for a strong ion signal. Thus the question arises; can we reduce ion fragmentation by reducing the energy of the VUV photon, or is the fragmentation an inevitable consequence of the vaporization process? For instance, Amirav *et al.*[26,27] concluded that the fragmentation in electron impact could be dramatically reduced by cooling the sample in a molecular beam, thereby suggesting that the molecule's internal energy is a decisive factor in the fragmentation process. LaFranchi *et al.* have recently employed photoelectron resonance capture ionization (PERCI) to reduce fragmentation.[28,29] A similar reduction is possible with chemical ionization [20,21] In this paper, we address this issue by generating light at 8.75 eV, which is nearly 2 eV lower than the previously used 10.48 eV. The nature of the vaporization method of oleic acid particles is also explored to better understand how different vaporization conditions affect the oleic acid mass spectrum.

2.2. Experimental Approach

The current experimental set-up can be seen in Figure 2.1. The oleic acid particles in this study were generated by atomizing a 1:10 oleic acid:isopropanol mixture with a glass nebulizer (Meinhard). The particles were then sent into an aerodynamic lens as described by Liu *et al.*,[30,31] where they were focused and accelerated by gas expansion into the

vacuum. The particle velocity, and thus their size, was determined by detecting scattered light as they passed through two green, continuous laser beams. The scattered light signals were sent into a timing circuit, which triggered the CO_2 laser to fire as the particle reached the TOF extraction region. After a variable delay between 2 – 20 μs, the vapor plume was ionized via VUV irradiation (λ=142 nm).

The VUV radiation was generated by resonance difference frequency mixing (RDFM) as shown in Figure 2.2.[32] The 355 nm output from a Nd:YAG laser (Continuum) pumped a dye laser (Continuum) with an Exalite 428 dye to produce 425 nm light. This light was doubled with a BBO crystal in an Inrad Autotracker III, yielding λ = 212.5 nm light. The λ = 425 nm (2 mJ) and 212.5 nm (10 mJ) pulses were steered through a series of prisms, and directed into a Kr cell (P_{Kr} = 10 torr) where RDFM produces the desired 142 nm (8.75 eV) light. The exit of the mixing cell was terminated by a LiF lens with a focal length of 20 cm, which causes the 142 nm light to slightly converge, leaves the 212 nm light nearly parallel, and the 425 nm light slightly divergent. This arrangement minimized the absorption of the 212.5 nm and 425 nm light by the ion. Future experiments will pass the output through a LiF wedge prism to completely eliminate the lower energy photons from the ionization region.

The ions generated by the VUV light were accelerated out of the ionization region by a DC extraction field and into the flight tube after which they were detected by a pair of

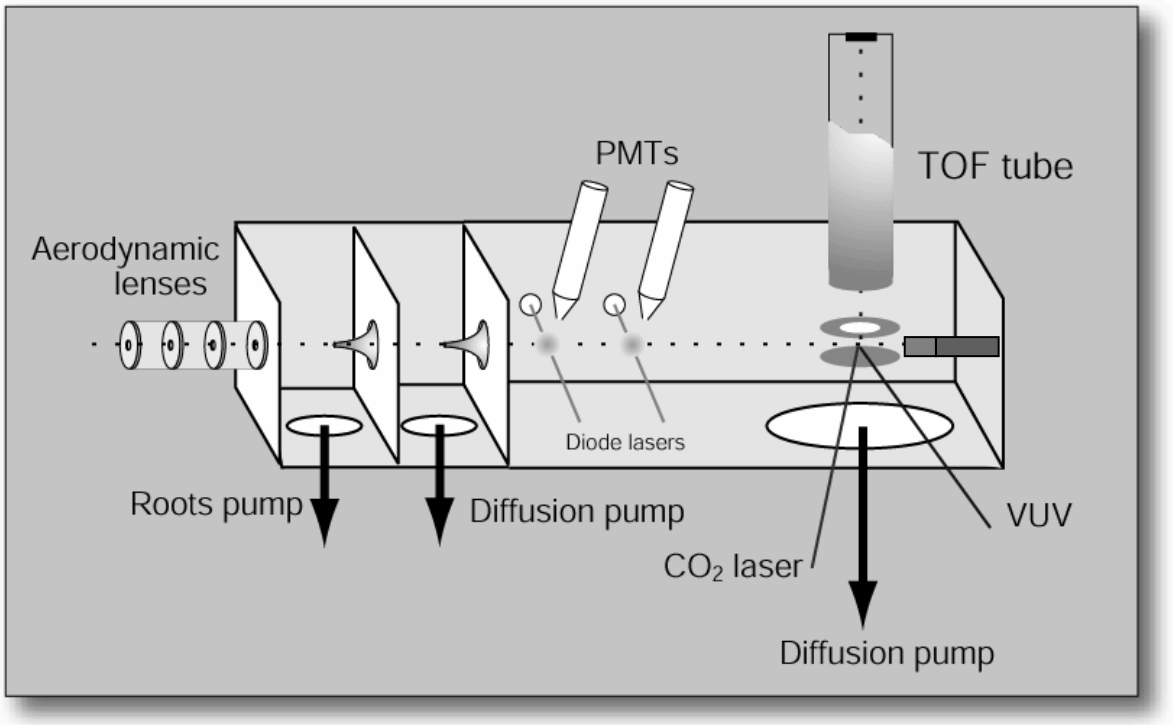

Figure 2.1: Schematic of single aerosol particle laser TOF instrument. Particles are focused in the aerodynamic lens, detected and sized in the two light scattering regions, then vaporized and ionized in the extraction region of the TOF-MS.

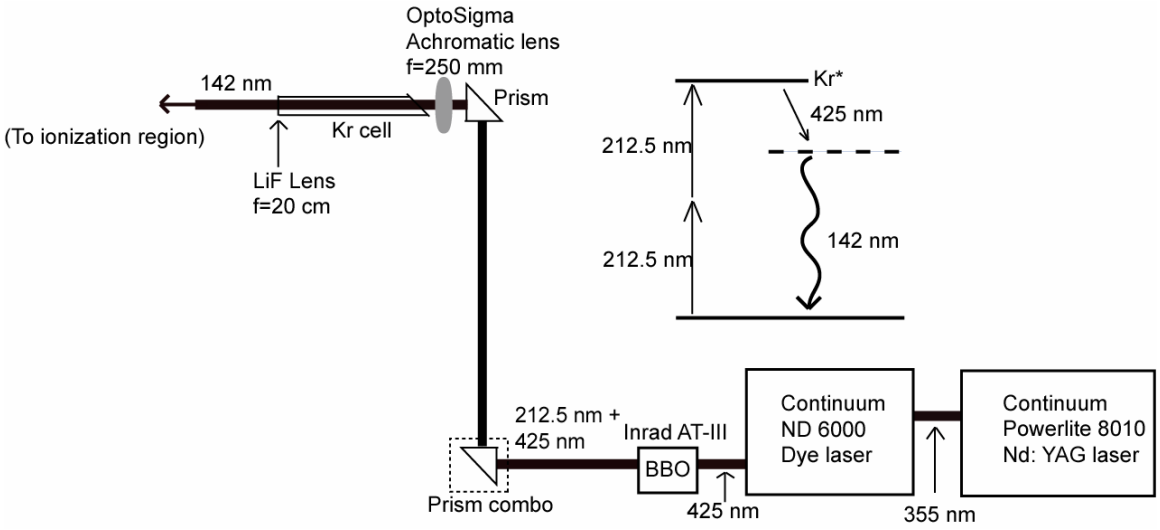

Figure 2.2: Schematic of resonance difference frequency mixing (RDFM) set-up. Both $\lambda = 425$ nm and $\lambda = 212.5$ nm enter the Kr mixing cell, and the resultant 142 nm light is then focused into the main chamber via a LiF lens.

multichannel plates (MCPs). Each firing of the CO_2 and VUV lasers produced a complete single particle mass spectrum on a digital oscilloscope (HP, Infinium), which digitized each mass spectrum and transferred it to a PC through a GPIB connection. Though the particles produced with the nebulizer were polydisperse, the timing circuit that controls the firing of the CO_2 and VUV (or just the VUV in the case of heater vaporization) lasers was adjusted to only trigger on 3 – 4 μm particles. The total count rate of particles of all sizes was sufficiently low (ca 20 per second) that the uncounted particles were pumped away long before the size selected particles were analyzed so that they did not interfere with the analysis. Typically a mass spectrum was recorded by averaging 100 single particle mass spectra.

A threshold photoelectron photoionization coincidence (TPEPICO) study of oleic acid was undertaken in order to examine the ionization energy of oleic acid and the onset

energies of its fragment species. Ions are energy selected by TPEPICO, which collects mass spectra of ions in coincidence with their zero-energy electrons, yielding information on fractional abundance of parent and daughter ions as a function of the photon energy. The apparatus has been described in detail elsewhere.[33,34] Briefly, a gaseous sample was directly introduced into the ionization region of the mass spectrometer. Because of the low vapor pressure of oleic acid at room temperature, it was necessary to introduce the sample with a heated inlet of approximately 430 K as monitored by a thermocouple. The oleic acid sample was ionized with VUV light from a H_2 discharge lamp, dispersed by a 1m normal incidence monochromator. Electrons and ions were continuously extracted in opposite directions by a 20V/cm field. The electron signal collected by a channeltron electron multiplier served as the start time for ion time-of-flight (TOF) collection, and the ion signal collected with a multichannel plate detector served as the stop time for the ion. Each coincidence event was stored on a multichannel pulse height analyzer. Low sample signal made it necessary to collect spectra for periods on the order of hours at each wavelength.

2.3 Results and Discussion

Figure 2.3 shows a comparison of an oleic acid mass spectrum taken with 118 nm light and one taken using the RDFM wavelength of 142 nm (8.75 eV). The amplitude of the m/z=282 peak is approximately eight times higher for the spectrum obtained via RDFM than for the 118 nm case. This is partly a result of the reduced fragmentation in the RDFM case. With the 142 nm light, the only fragment observed is due to water loss, yielding a peak at m/z=264. Reduced fragmentation not only allows for easier identification of m/z=282, but the absence of other fragments greatly facilitates the analysis of mixtures.

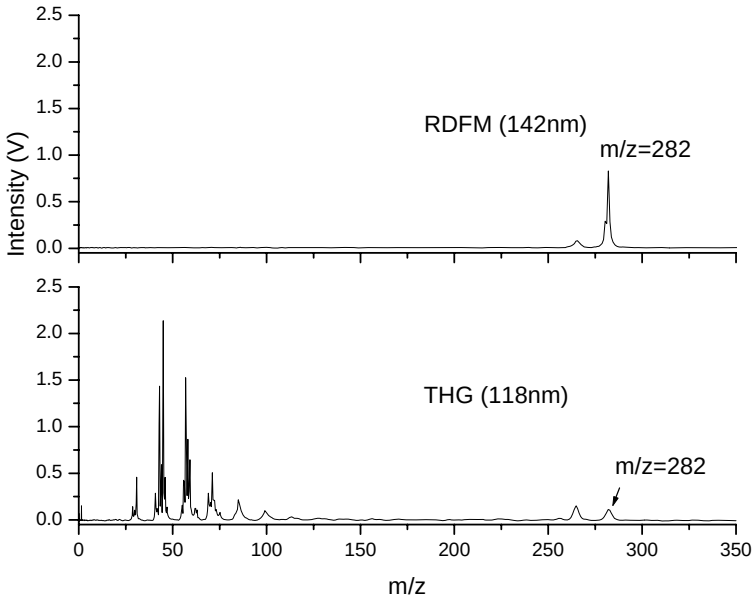

Figure 2.3: Oleic acid spectra obtained with a CO_2 laser power of 70 mJ/pulse and VUV wavelengths of a) 142 nm and b) 118 nm. The vertical axis is the ion signal measured as a voltage on the oscilloscope.

No literature value for the ionization energy of oleic acid exists. However, the strong mass spectral signal observed with 8.75 eV laser ionization indicates that its IE is less than this.

Photoionization at various wavelengths was used to determine that the ionization energy of oleic acid is 8.6$\pm$0.1eV. The breakdown diagram of oleic acid in Figure 2.4 shows fractional abundances of the molecular ion, m/z=282, and two daughter ions, m/z=264 and m/z=256 as a function of VUV photon energy. In order to obtain the ion energy from the photon energy, it is necessary to add to the photon energy the ion internal energy, which depends on the temperature of the experiment (430 K in this case). If the temperature of the CO_2 laser vaporized aerosol particle were similar to the temperature of the TPEPICO experiment, the 8.75 eV VUV photon ionization should yield only the parent ion. The fact

that we observe a water loss peak indicates that the laser vaporized molecules have a higher internal temperature than the gas phase oleic acid molecules vaporized at 430 K.

The onset for water loss signal in the breakdown diagram of Figure 2.4 appears at about 9.1 eV. However, the ion TOF distributions indicate that at this energy, the parent ion is metastable and loses water slowly. The true thermochemical dissociation limit may lie well below 9.1 eV, but no fragment ions are observed because the low dissociation rate constant does not permit the ion to dissociate on the timescale of the ion TOF collection, which is on the order of 20 μs. This effect causes the fragment appearance energy of 9.1 eV to be higher than its true thermochemical dissociation energy. On the other hand, the ions initially contain considerable thermal energy as a result of heating the sample to 430 K. This causes the appearance energy (observed onset) of the water loss peak to be shifted toward lower energy. Without a detailed analysis that takes calculated dissociation rate constants and the thermal energy distribution into account, it is indeed difficult to determine a precise dissociation energy for the water loss peak. An approximate dissociation energy is 9 eV.

2.3.1 The effect of CO_2 laser power and VUV laser delay

Figure 2.5 relates the CO_2 laser power to the total mass spectral signal. Initially, the total oleic acid spectral area increases with increasing CO_2 laser power as more of the particle is vaporized. At a CO_2 power of approximately 173 mJ/pulse, the total oleic acid signal begins to plateau, an effect similar to that seen by Woods *et al.* in their study of *m*-nitrotoluene particles.[3] This leveling of the spectral area is an indication that laser heating results in complete vaporization. For this experiment, the delay between the application of the CO_2 and VUV laser pulses was adjusted to achieve optimal signal intensity. This was

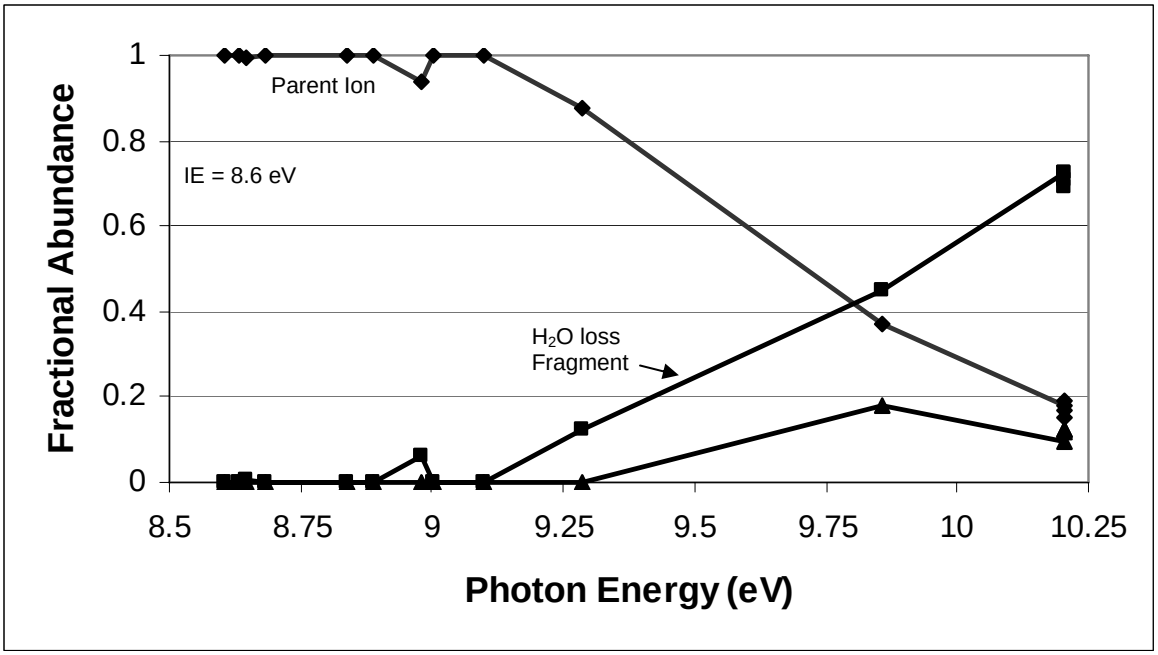

Figure 2.4: The fractional abundance of parent and two fragment ions for energy selected oleic acid ions prepared by threshold photoelectron photoion coincidence (TPEPICO)

necessary because the translational energy of the vaporized molecules increases with the CO_2 laser power, thus necessitating the reduction of the delay between the two lasers.

As shown in Figure 2.5, the maximum relative intensity for the oleic acid parent peak (m/z=282) is located at ~75 mJ/pulse. The maximum of the m/z=264 intensity, which occurs at ~173 mJ/pulse is coincident with the location of the threshold power. This suggests that up to 173 mJ/pulse, the CO_2 laser puts only enough excess internal energy into the vaporized oleic acid molecules to produce m/z=264 when the molecule is ionized with VUV irradiation. At powers greater than 173 mJ/pulse, both the parent peak and the m/z=264 peak decrease with increasing CO_2 laser power. After ~200 mJ/pulse however, the total oleic acid mass spectral area begins to increase, possibly as a result of the dissociation of neutral oleic acid into two fragments, both of which can be ionized by the VUV laser. At lower CO_2 laser

powers where the oleic acid ion primarily loses just water, only the m/z=264 fragment can be ionized by the 8.75 eV VUV laser, while the water fragment cannot.

a)

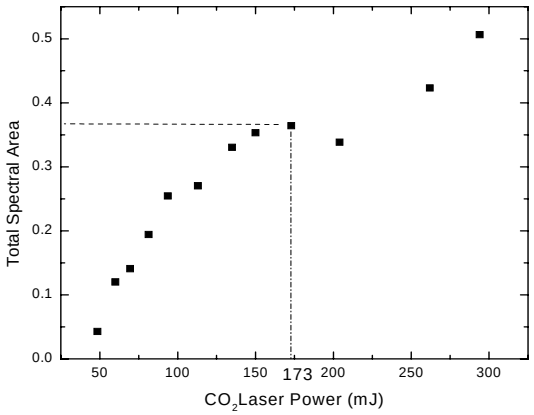

b)

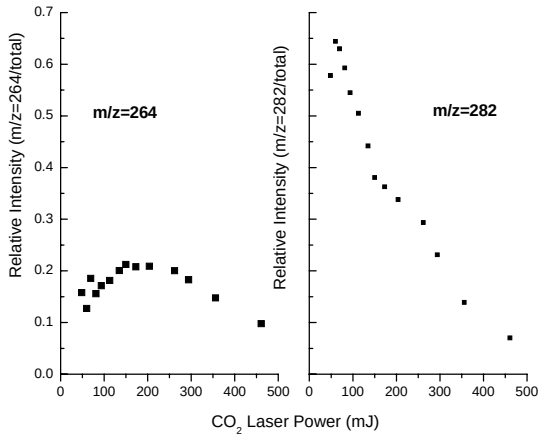

Figure 2.5: a) Total mass spectral intensity as a function of CO_2 laser power for oleic acid. The dashed vertical line represents the threshold power for complete particle vaporization. b) Plot of m/z=264 and m/z=282 relative intensities with respect to CO_2 power.

One of the interesting questions deals with the mechanism for fragment ion production. Two scenarios could account for their observation:

$$\text{Oleic acid} \xrightarrow{h\nu(CO_2)} \text{neutral Fragments} \xrightarrow{h\nu(VUV)} \text{Fragment ions} \qquad (2.1)$$

$$\text{Oleic Acid} \xrightarrow{h\nu(CO_2)} (\text{Oleic Acid})^* \xrightarrow{h\nu(VUV)} \text{Fragment ions} \qquad (2.2)$$

In the first case, the CO_2 laser dissociates the oleic acid into neutral fragments, which are then ionized by the VUV laser. In the second mechanism, the CO_2 laser just heats up the oleic acid, and the fragment ions are produced by dissociative ionization. In general, the second mechanism is more likely because ionic species have lower dissociation energies than neutral species. But, given sufficient CO_2 laser power, it is possible that both mechanisms pertain here. The increase in the total ion signal after about 200 mJ of CO_2 laser power seen in Figure 2.5 can be accounted for by mechanism (2.1) because the dissociation of the neutral oleic acid generates multiple fragments that are candidates for ionization by the VUV laser, whereas mechanism (2.2) will only generate one ion.

In an effort to distinguish the effects of mechanisms 2.1 and 2.2, the CO_2-VUV delay time was varied for several different CO_2 laser powers. At each laser power, as the delay time increased, the ratio of the (m/z =282)/(m/z=264) peak areas also increased. The effect is even more dramatic at 294 mJ IR laser power. At long delay times, the lower mass fragments are nearly absent, whereas they are dominant at 4 μs delay time. The interpretation of the changing mass spectra as a function of the VUV laser delay depends on whether mechanism (2.1) or (2.2) is operative. Suppose that mechanism (2.1) is dominant so that the observed fragment peaks in Figure 2.6 originate from the ionization of neutral fragments. If particles were heated and vaporized homogeneously, all molecules (fragments and parent molecules) would have the same temperature and thus the same translational energy distribution. But, the neutral fragments would have a higher velocity as a result of

their lower mass. The VUV laser has a focal region of about 3 mm^2. The center of the VUV laser spot is offset from the center of the CO_2 by ~ 1 mm, and the aerosol particle therefore requires some time to expand to fill the VUV spot after vaporization. Fast fragments might therefore arrive before the heavier parent molecules. However, calculated Maxwell-Boltzmann distributions of molecular velocities for each ion species at several different temperatures show that the difference in the velocity between the m/z=264 fragment and the m/z=282 parent is so small that it cannot account for the large change in the ion intensities at for instance 294 mJ (Figure 2.6). Nor can the large intensity of the smaller fragments at short times be accounted for in this manner.

The second mechanism, in which the CO_2 laser simply heats the oleic acid and the fragment ions are generated by dissociative ionization, is also not consistent with a single temperature for the sample. In this mechanism, all mass spectra should have the same mass peaks in the same relative proportions independent of the VUV laser delay time because the ion precursor is always the parent molecule.

Because of this non-uniform temperature, we cannot distinguish mechanism (1) and (2) on the basis of the data in Figure 2.6. The only evidence for mechanism (1) is the increased ion signal as observed in Figure 2.5a.

Two sources of non-uniform temperatures can be postulated. It is possible that the laser does not heat the particle uniformly so that parts of the particle are hotter than others. As pointed out by Woods *et al.*[3] the time required for the thermal equilibration of a 2 μm particle is on the order of 10 μs. This is longer than the time required to vaporize the particle, so that the non-uniform distribution of temperatures could be transferred to the vapor phase. The hot parts of the particle would eject their vapor more rapidly thus

accounting for the change in the mass spectra with IR-VUV laser delay times. It is also possible that even if the particle is initially heated uniformly, the vaporization process itself can cool the particle during the course of evaporation. That is, while "hot" molecules are ejected from the surface of the particle, the expansion of the particle itself can lead to cooling of interior molecules, thereby generating a temperature gradient during the course of evaporation.

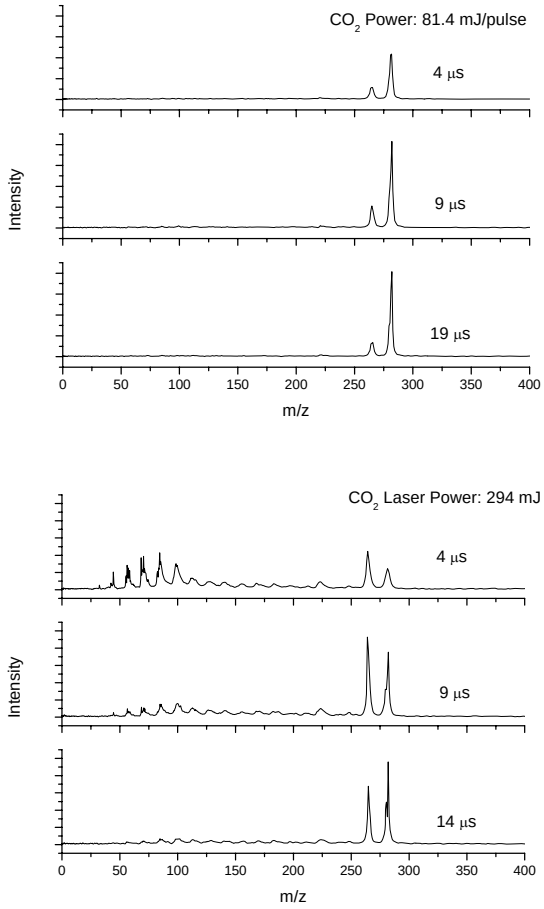

Figure 2.6: Oleic acid spectra at various CO_2 powers and CO_2-VUV delay times. The vertical axes are the same for each spectrum within the given CO_2 power. The m/z=282 signal is ~0.5V for the 14 μs delay at 294 mJ, and ~0.8V for the 19 μs delay at 81.4 mJ.

Molecules and/or fragments detected at a delay time of 14 μs were calculated to have a temperature of ~57 K, while those detected at a delay of 4 μs had a calculated temperature of ~700 K. Therefore, species detected at shorter delay times are "hotter" and possess more vibrational energy than the "colder" species detected at longer delays, thereby accounting for the degree of fragmentation as a function of delay time, and thus the changing (m/z =282)/(m/z=264) ratio. It is likely that mechanism (2.1) is dominant at high CO_2 laser powers.

2.3.2 Use of Heater with VUV laser

In a previous study[35], we showed that aerosol particles can also be vaporized by letting them impinge on a heater, as is done in the instrument of Jayne *et al.*[19] In our case, oleic acid particles fly through the ionization region, hit the heater and are vaporized, and travel back to the ionization region before being ionized by the VUV laser. So, for a particle with an incoming velocity of 100 m/s before vaporization, and a resultant vapor molecule velocity of 220 m/s (at a 640 K heater temperature), it takes a particle on the order of 60 μs to arrive at the heater after first crossing through the extraction region, and on the order of 30 μs for resulting vapor molecules to return to the extraction region for ionization. Figure 2.7 shows an example of an oleic acid particle mass spectrum taken using the heater for particle vaporization.

Contrary to vaporization using a CO_2 laser, use of a cartridge heater provides homogeneous heating of oleic acid particles. As mentioned, the mean velocity of m/z=264 and m/z=282 molecules are very similar at a given temperature. Therefore, if particles are

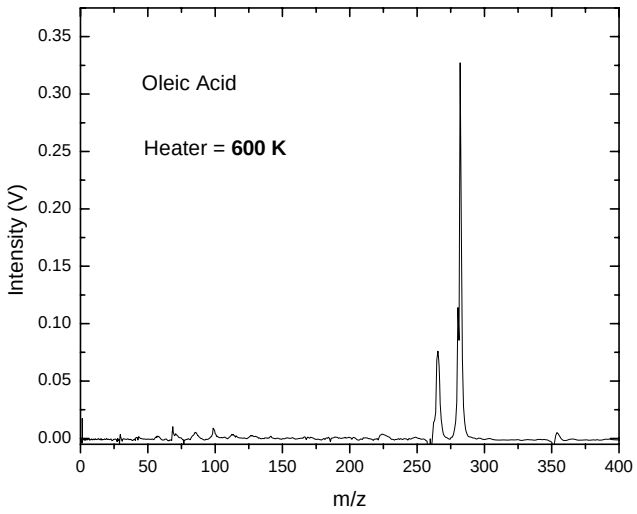

Figure 2.7: Oleic acid particle mass spectrum taken with the cartridge heater at 600K. Background signal has been subtracted.

indeed heated homogeneously, a constant ratio of (m/z=264)/(m/z=282) should be expected independent of VUV delay, as indeed observed experimentally in Figure 2.8.

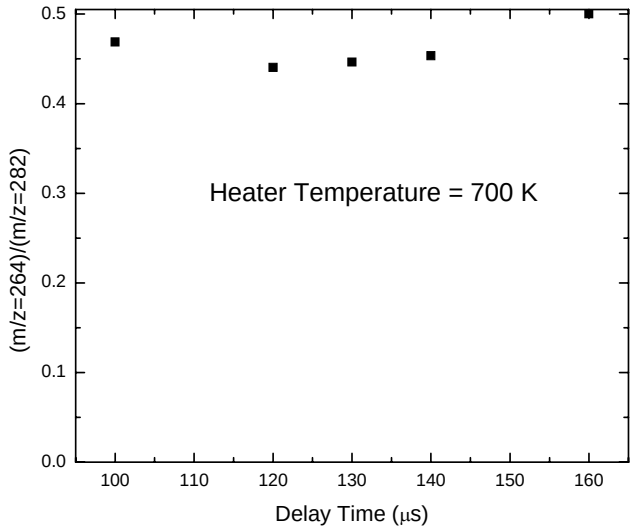

Figure 2.8: (m/z=264)/(m/z=282) ratio as a function of VUV delay time using a cartridge heater for the vaporization step.

Given that the heater provides homogeneous particle heating, calculation of the average energy of oleic acid ions as a function of temperature was performed to try to understand the fragmentation pattern upon ionization at the vaporization temperatures used in this experiment (Figure 2.9).

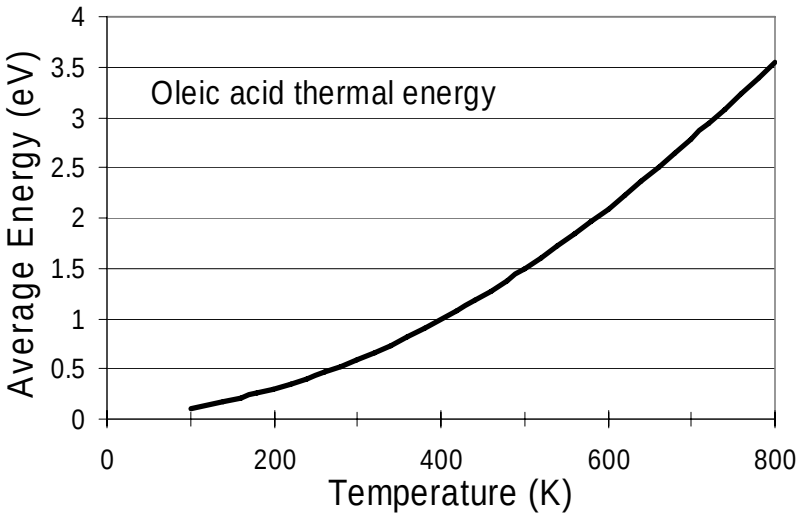

Figure 2.9: Calculated average oleic acid internal energy as a function of temperature using the calculated oleic acid vibrational frequencies.

These average energy calculations indicate that at 700 K, oleic acid has an internal energy of approximately 2.7 eV. When these molecules are ionized by an 8.75 eV photon, the ion can be generated in a range of energies from the ionization energy of 8.6 eV to 11.45 eV. According to the breakdown curve in Figure 4, this should result in substantial fragmentation of the ions. But the observation of fragment ions depends upon the time scale of the experiment because of the low dissociation rate constants. The breakdown diagram in Figure 2.4 was taken with a 20 V/cm extraction field and the ions were accelerated over a 5 cm region, whereas in the aerosol experiment, the extraction field was 200 V/cm and the

extraction distance was just 1 cm. Thus, the time to extract an ion of mass 282 is 12.1 μs in the TPEPICO case and 1.7 μs in the aerosol instrument. That is, the ions have a residence time of 7.1 times longer in the TPEPICO instrument than in the aerosol instrument. By delaying the extraction pulse in the aerosol instrument, we can lengthen this residence time and thus increase the fragment ion signal. This is verified in Figure 2.10 where the ratio of parent to daughter ion signal changes from 1.72 to 1.27 as the delay time is increased from 0 to 3 μs. That is, the longer we wait before extracting the ions, the more time is provided for the ion to dissociate. These data were corrected for a background signal discussed in the following section.

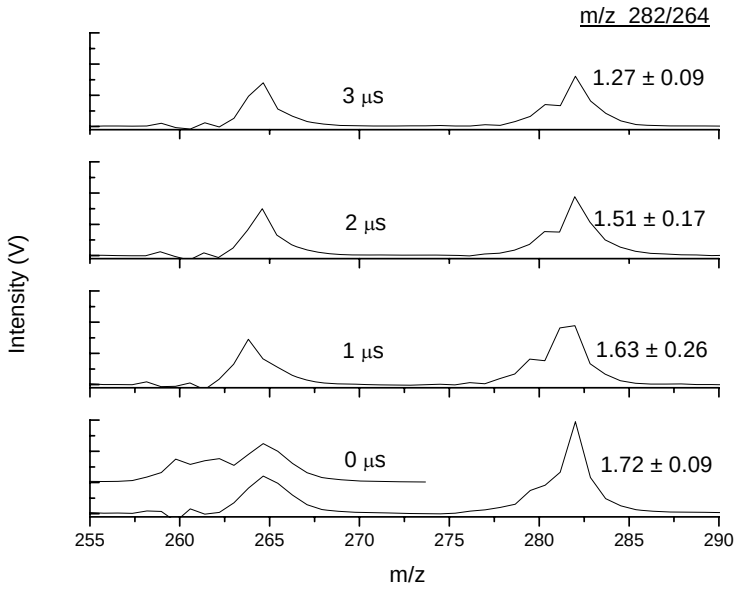

Figure 2.10: The mass spectra of oleic acid particles at a heater temperature of 700K at the pulsed extraction delay times indicated in the figure. The ratio of (m/z=282)/(m/z=264) peak areas is shown on the right for each delay time. The variation of this ratio with pulsed extraction delay is a reflection of the slow dissociation of the parent oleic acid ion.

Background signals (Figure 2.11) have been subtracted from the spectra in this figure. For comparison, the raw particle spectrum before background subtraction for 0 μs delay is vertically offset from the background subtracted spectrum. Additionally, it should be noted that the vertical axis for each of the spectra in this figure are the same.

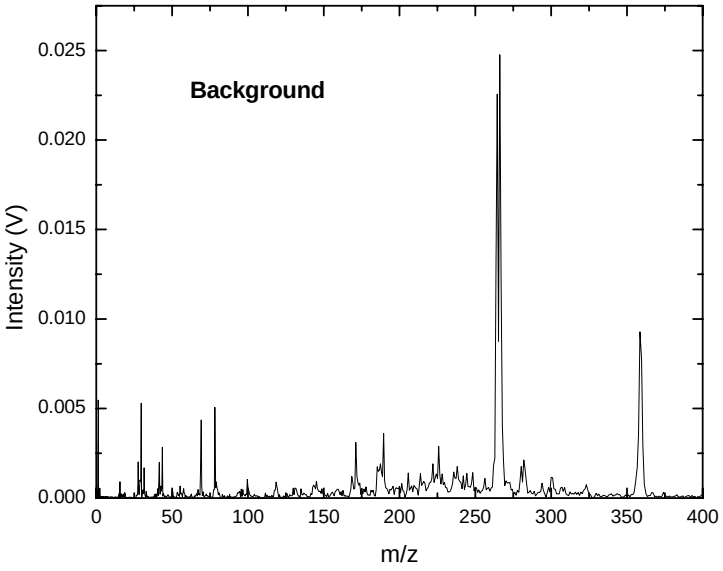

Figure 2.11: Background signal without particles. Obtained using only the VUV laser.

2.3.3 Comparison of particle evaporation by heater and CO_2 laser

Overall, the heater is preferential to the CO_2 laser because it heats particles homogeneously, and as such, yields similar parent/fragment ratios across a range of VUV delay times. One drawback with the heater is that the overall intensity is lower because the heater tip can only be placed within approximately 6 mm from the center of the extraction region. Calculations show that this distance from the extraction region should cause signal obtained with heater vaporization to be ~ 2.8 times lower than signal obtained using the CO_2

laser. These calculations involved determining the percentage of the vapor plume that would be contained within the VUV laser spot area for each vaporization method. Comparison of the signal level for an oleic acid mass spectrum collected with a CO_2 power of 81.4 mJ with a mass spectrum collected with a heater temperature of 640 K showed a CO_2 signal/heater signal ratio of ~3.2, which is close to the predicted ratio of 2.8.

An interesting feature common in all spectra taken in this study is the background signal (Figure 2.11). This spectrum was obtained by firing the laser at a time when no particle is passing through the ionization region. It is evident that this spectrum looks completely different from the particle mass spectrum in that the oleic acid peak at 282 is barely visible. On the other hand, a new peak appears (actually a doublet at m/z 258 and 261) which does not line up with the water loss peak at 264. The origin of this background was determined to be a result of the residual 212 nm light that is co-propagating with the VUV light. Because the peaks do not line up with the water loss peak, it was rather easy to subtract its contribution from the data in Figure 2.10. Efforts are currently underway to solve this problem by introducing a LiF wedge prism into the experimental set-up, which will separate the 212 nm light from the 142 nm light, preventing the 212 nm light from entering the ionization chamber.

The set-up used in this study shows great promise for the study of heterogeneous gas-particle reactions. The increased signal that is obtained through the RDFM ionization scheme will allow for the study of coated particles.[18,3] These types of particles are important in the effort to distinguish uptake that occurs due to surface vs. bulk reaction between a particle and gas phase species such as ozone or OH radicals. Additionally, real atmospheric particles are more likely to be mixtures of different compounds. Therefore, the

use of an ionization method with a photon energy much closer to the ionization potential of most organic species than the 118 nm photon previously used will give less fragmentation. This will enhance the ability to study compounds in complex mixtures. The current set up is limited to a single wavelength of 142 nm because only a single dye laser is used to generate the 212 nm precursor and the 425 nm difference frequency. With a second dye laser the 425 nm light currently used to down shift the output photon, can be made variable so that variable energy VUV light in this region can be generated. This would allow the VUV light energy to be tuned close to the ionization energy of specific compounds in the mixture so that they may be studied individually. On the other hand, the additional complexity of a tunable source would prohibit its use as a portable instrument in the field. The ideal approach for multi-component analysis is clearly MS/MS and an attempt at such an approach has been tried.[36]

2.3.4 The use of rare gas resonance lamps

Although the RDFM method is extremely effective in a laboratory environment, the size of the set-up and the delicate aspects of laser alignment prevent it from being used in portable field instruments. An attractive alternative is the use of rare gas resonance lamps.[37] Kr (10.0 eV) and Xe (8.4 eV) lamps can be produced in a compact format (Syagen Inc.) and should provide up to 10^{15} photons per second. If these photons can be effectively directed into the ionization region, such lamps should produce the same signal as pulsed lasers. A flux of 10 particles per second with a 1 μm diameter (or 10^4 particles per second with a diameter of 100 nm) would produce a mass flow of 4.2×10^{-12} g/sec assuming a particle density of 0.80 g/cm^3. Because the gas flow into the aerodynamic lens of our instrument is about 1 cc/sec, such a mass flux would be generated by an atmospheric particle density of 4.2 μg/m^3, which is a reasonable density for clean atmospheres (typical urban

atmospheres have a density of ~20-100 $\mu g/m^3$).[17] If the particles are vaporized and generate oleic acid molecules with a mean velocity of $2x10^4$ cm/sec, and the gas is returned in a 1 cm^2 cross sectional area, the average gas density in the ionization region will be $4.5x10^5$ oleic acid molecules/cm^3. Given a photoionization cross section of 10^{-18} cm^2 and a photon flux of 10^{15} photons/sec, the expected signal level is about 500 ions per second.

There is a major difference in the predicted ion signals of the continuous and pulsed light sources. For a large particle flow (1 μm diameter) of 10 particles per second, the pulsed laser with its 10^{10} photons per pulse can be efficiently used because it is fired only when a substantial gas density is generated by the arrival of a large particle. We expect that the peak gas density will be higher by a factor of 3000 thereby generating ions at the rate of 150 ions per second, even though the photon flux is only 10^{10} photons per pulse. This estimate is actually lower than our experimental signal, perhaps a result of our conservative estimation of the ionization cross section.

These calculations show that the signal levels for a flow of 1 μm particles is about the same for the pulsed laser operating with 10^{10} photons per pulse and the continuous source with 10^{15} photons per second. However, if the particles are small, the pulsed laser loses its efficiency and its low photon flux prevents its use. The continuous source of 10^{15} photons per second, on the other hand, is equally efficient (or inefficient) for particles of any size and depends only on the total mass flux, and not on its temporal distribution.

2.4. Conclusion

The comparison between the 8.75 eV photons generated by resonance difference four-wave mixing (RDFM) and the 10.48 eV photons generated by third harmonic generation

(THG) demonstrates that the lower energy pulsed laser photons are much more effective in giving fragmentation free spectra of organic constituents of aerosol particles. The test was carried out with oleic acid, a molecule of interest in atmospheric chemistry. The reduced ion fragmentation also results in a stronger parent peak signal. The results indicate that infrared CO_2 laser vaporization, especially at high IR laser pulse energies, produces vapor with a non-uniform temperature distribution as evidenced by mass spectra that depend upon the IR/VUV laser delay time. We suggest that this is a result of either non-uniform heating of the aerosol particle by the CO_2 laser, or of particle cooling as the outer layers of the particle vaporize. Using a heater for the vaporization step provides a more homogeneous temperature profile within the particles. In both cases, the dissociation of oleic acid is shown to be slow on the timescale of the experiment, which suggests that fragmentation free mass spectra are more likely if the ions are quickly extracted from the ionization region. Work is currently being done on the experiment to spatially separate λ=142 nm and λ=212 nm to prevent any 1+1 REMPI from occurring, which should further decrease the intensity of the m/z=264 water loss peak. Finally, we show that a continuous lamp with a photon flux of about 10^{15} photons per second should be an ideal ionization source for the detection of organic species in large and small aerosol particles.

Acknowledgements

We thank the National Science Foundation and the Air Force Office of Scientific Research (AFOSR) for financial support. We also thank Profs. John Hepburn and Myungsoo Kim for help in setting up the resonance frequency difference mixing scheme.

References

[1] M.V. Johnston, A. S. Wexler, Anal. Chem. 67 (1995) 721A.

[2] K.R. Neubauer, M. V. Johnston, A. S. Wexler, Int. J. Mass Spectrom. Ion. Proc. 163 (1997) 29.

[3] E. Woods III, G. D. Smith, R. E. Miller, T. Baer, Anal. Chem. 74 (2002) 1642.

[4] E. Woods III, G. D. Smith, Y. Dessiaterik, T. Baer, R. E. Miller, Anal. Chem. 73 (2001) 2317.

[5] P.T.A. Reilly, A. C. Lazar, R. A. Gieray, W. B. Whitten, J. M. Ramsey, Aerosol Sci. Technol. 33 (2000) 135.

[6] M. Yang, P. T. A. Reilly, K. B. Boraas, W. B. Whitten, J. M. Ramsey, Rapid Comm. Mass. Spectr. 10 347.

[7] K.A. Prather, T. Nordmeyer, K. Salt, Anal. Chem. 66 (1994) 1403.

[8] Z. Ge, A. S. Wexler, M. V. Johnston, Environ. Sci. Technol. 32 (1998) 3218.

[9] A.M. Middlebrook, D. M. Murphy, S.-H. Lee, D. S. Thompson, K. A. Prather, R. J. Wenzel, D.-Y. Liu, D. J. Phares, K. P. Rhoads, A. S. Wexler, M. V. Johnston, J. L. Jimenez, J. T. Jayne, D. R. Worsnop, I. Yourshaw, J. H. Seinfeld, R. C. Flagan, J. Geophys. Res. 108 (2003) SOS 12/1.

[10] D.S. Gross, M. E. Galli, P. J. Silva, S. H. Wood, D. Y. Liu, K. A. Prather, Aerosol Sci. Technol. 32 (2000) 152.

[11] L.S. Hughes, J. O. Allen, P. Bhave, M. J. Kleeman, G. R. Cass, D. Y. Liu, D. P. Fergenson, B. D. Morrical, K. A. Prather, Environ. Sci. Technol. 34 (2000) 3058.

[12] M.R. Alfara, H. Coe, J. D. Allan, K. N. Bower, H. Boudries, M. R. Canagaratna, J. L. Jimenez, J. T. Jayne, A. A. Garforth, S. M. Li, D. R. Worsnop, Atmos. Environ. 38 (2004) 5745.

[13] Q. Zhang, C. O. Stanier, M. R. Canagaratna, J. T. Jayne, D. R. Worsnop, S. N. Pandis, J. L. Jimenez, Environ. Sci. Technol. 38 (2004) 4797.

[14] M.R. Canagaratna, J. T. Jayne, D. A. Ghertner, S. Scott, Q. Shi, J. L. Jimenez, P. J. Silva, P. Williams, T. Lanni, F. Drewnik, K. L. Demerjian, C. E. Kolb, D. R. Worsnop, Aerosol Sci. Technol. 38 (2004) 555.

[15] D.J. Cziczo, D. M. Murphy, P. K. Hudson, D. S. Thomson, J. Geophys. Res. 109 (2004)

[16] D.J. Cziczo, D. M. Murphy, D. S. Thomson, M. N. Ross, Geophys. Res. Lett. 29 (2002) 33/1.

[17] B. J. Finlayson-Pitts, J. N. Pitts, Chemistry of the Upper and Lower Atmosphere: Theory, Experiments and Applications, Academic Press, New York, 2000.

[18] Y. Katrib, S. T. Martin, H. M. Hung, Y. Rudich, H. Zhang, J. G. Slowik, P. Davidovits, J. T. Jayne, D. R. Worsnop, JCPA 108 (2004) 6686.

[19] J.T. Jayne, D. C. Leard, X. Zhang, P. Davidovits, K. A. Smith, C. E. Kolb, D. R. Worsnop, Aerosol Sci. Technol. 33 (2000) 49.

[20] J.D. Hearn, G. D. Smith, Anal. Chem. 76 (2004) 2820.

[21] J.D. Hearn, G. D. Smith, J. Phys. Chem. A 108 (2004)

[22] P.J. Silva, K. A. Prather, Anal. Chem. 72 (2000) 3553.

[23] K. Salt, C. A. Noble, K. A. Prather, Anal. Chem. 68 (1996) 230.

[24] B. Oektem, M.P. Tolocka, M.V. Johnston, Anal. Chem. 76 (2004) 253.

[25] G.D. Smith, E. Woods III, C. Hauser, R. E. Miller, T. Baer, J. Phys. Chem. A 106 (2002) 8085.

[26] A. Amirav, J. Phys. Chem. 94 (1990) 5200.

[27] A. Amirav, A. Danon, Int. J. Mass Spectrom. Ion. Proc. 97 (1990) 107.

[28] B.W. LaFranchi, G.A. Petrucci, J. Am. Soc. Mass Spectrom. 15 (2004) 424.

[29] B.W. LaFranchi, J. Zahardis, G.A. Petrucci, Rapid Commun. Mass Spectrom. 18 (2004) 2517.

[30] P. Liu, P. J. Ziemann, D. B. Kittelson, P. H. McMurry, Aerosol Sci. Technol. 22 (1995) 293.

[31] P. Liu, P. J. Ziemann, D. B. Kittelson, P. H. McMurry, Aerosol Sci. Technol. 22 (1995) 314.

[32] J.W. Hepburn, in: A.B. Myers, T.R. Rizzo (Eds.), Laser Techniques in Chemistry, John Wiley and Sons, Inc., New York, (1995) pp. 149-183.

[33] T. Baer, J. A. Booze, K. M. Weitzel, 1 (1991) 259.

[34] B. Sztáray, T. Baer, Rev. Sci. Instrum. 74 (2003) 3763.

[35] C. Sykes, E. Woods III, G. D. Smith, T. Baer, R. E. Miller, Anal. Chem. 73 (2001) 2048.

[36] R.A. Gieray, P.T.A. Reilly, M. Yang, M.B. Whitten, J.M. Ramsey, Anal. Chem. 70 (1998) 117.

[37] J. A. R. Samson, Techniques of Vacuum Ultraviolet Spectroscopy, Wiley, New York, 1967.

CHAPTER 3

The Uptake of O_3 by Myristic Acid/Oleic Acid Mixed Particles: Evidence for Solid Surface Layers

The oleic acid ozonolysis in mixed oleic and myristic acid particles was studied in a flow tube reactor using single particle mass spectrometry. The change in reactivity was investigated as a function of the myristic acid concentration in these 2 micron particles. For pure oleic acid aerosol, the reactive ozone uptake coefficient, γ, was found to be 3.4 ($\pm$ 0.3) x 10^{-4} after taking secondary reactions into account. At the myristic acid crystallization point, where only 20% of the myristic acid is in the solid phase, the uptake coefficient was reduced to 9.7 ($\pm$ 1.0) x 10^{-5}. This dramatic drop in the uptake coefficient is explained by the presence of a crystalline monolayer of myristic acid, through which ozone diffusion is reduced by several orders of magnitude, relative to liquid oleic acid. Scanning electron microscope images of the mixed particles confirm that the particle surface is crystalline when the myristic acid mole fraction exceeds 0.125. The findings of these experiments illustrate that particle morphology is important to understanding the reactivity of species in a mixed particle. The decay of myristic acid during the course of ozonolysis is explained in terms of a reaction with stabilized Criegee intermediates, which attack the acidic groups of the oleic and myristic acids with equal rate constants.

3.1 Introduction

It is well known that aerosol particles affect the global energy balance.[1,2,3,4,5] Particles can directly affect the global climate by scattering and absorbing solar and terrestrial radiation.[6] The indirect effect results from the ability of particles to take up water, effectively acting as cloud condensation nuclei (CCN).[7,8,9,10]

Aerosol particles are also a public health issue. Particles can be inhaled and deposit in different areas of the respiratory system depending upon their size.[11,12,13] High atmospheric particulate concentrations have been linked to increased morbidity and mortality, especially in at risk groups such as infants and the elderly.[14,15,16,17,18]

Organic aerosol particles are reactive towards gas phase oxidants. These reactions affect the physicochemical properties of the aerosol, modifying their reactivity, their optical properties and shape. [19,20,21,22,23,24] For example, it has been found that organic particle oxidation enhances their ability to serve as cloud condensation nuclei [25] and increases particle toxicity.[26,27]

A number of heterogeneous aerosol chemistry studies have examined the reactivity of pure aerosol particles, especially the reaction between ozone and oleic acid.[28,29,30,31] However, real atmospheric particles are more likely to consist of complex mixtures of various components.[32,33,34,35,36,37,38,39] The reactivity of organic constituents can depend on the physiochemical properties of these mixtures.[40,41,42] For example, results from pure particle studies have estimated an oleic acid atmospheric lifetime on the order of minutes;[28] whereas field measurements indicate the lifetime is on the order of days.[33,43]

In order to link the laboratory and field measurements we must consider that an organic molecule such as oleic acid is mixed with many components. These species can

influence oleic acid oxidation by restricting its accessibility to ozone by crystallizing and limiting diffusion. A good starting point for examining this hypothesis is the reactivity of binary mixtures, especially those that change from liquid to solid phase as a function of the mixture composition.

To this end, the effect of phase changes on oleic acid oxidation have been examined with coated wall flow tube experiments.[44,45] In these investigations, the reactivity of pure oleic acid decreased by an order of magnitude upon crystallization on the wall of the flow tube. In another study, the ozonolysis reactivity of oleic acid in the binary mixture depended upon the method of film preparation, suggesting a dependence on crystal structure.[44]

The role of a condensed phase within an organic particle has also been studied.[46,24,31] Ozonolysis experiments were conducted with mixed oleic acid/hexadecanoic acid, and oleic acid/heptadecanoic acid particles. The presence of a solid impurity retarded the accessibility of ozone to the oleic acid, reducing the reaction rate.[31] On the other hand, Hearn and Smith[46] found that reaction rates remained high for myristic acid/oleic acid aerosols up to 87% myristic acid, despite exceeding the crystallization point. They concluded that the particles must have been supercooled. Supercooling was similarly invoked for mixed stearic acid/oleic acid particles [24]. The latter studies found a drop in reactivity by a factor of 3 or 4, respectively, upon the onset of crystallization.

The current study of the ozonolysis of oleic acid in binary mixtures serves as a complement to those that have recently been conducted. This provides an interesting comparison of the effect of particle size on the structure of crystallized particles, as super-micron particles are considered here. An advantage of using myristic acid as a second component with oleic acid is its crystallization point at X_{MA} ~0.10 (290 K).[47] At this

concentration, the aerosol particle is still ~90% oleic acid and dilution will play a minimal role in its decreased reactivity. This room temperature experiment is intended to isolate the effect of the solid matrix on the uptake coefficient. Thus, only changes in the phase of the constituents of the particle are involved in changes in the reaction rate. These results are cast in terms of previous work and lend insight about the morphology of the crystalline structure in aerosol particles.

3.2 Experimental Approach

The experimental set-up is shown in Figure 3.1. The particles, with a diameter of about 2 μm, were generated with a glass nebulizer (Meinhard, Golden, CO) by atomizing 10% solutions by volume of myristic acid/oleic acid in isopropanol. The isopropanol was removed by sweeping the particles through a drying tower with a flow of 800 sccm of argon. The particles then entered the 2.54 cm i.d., 1 m long reaction flow tube via a side port.

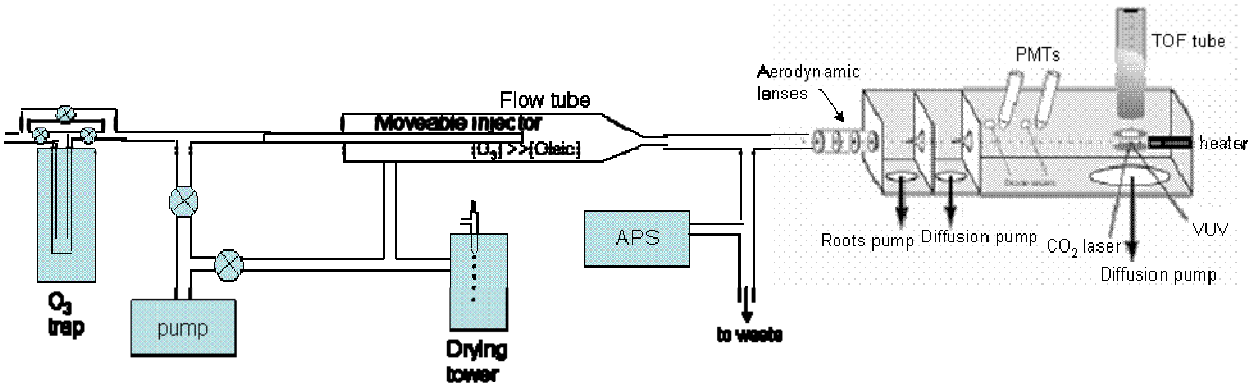

Figure 3.1: Schematic of experimental set-up for mixed particle experiments (not to scale).

Ozone was generated by flowing O_2 through an ozonizer (Pacific Ozone Technology, model L11, Benicia, CA). It was stored in a glass trap containing silica gel that was immersed in an acetone/dry ice bath. The ozone was carried out of the trap by a flow of

argon, diluted by a factor of 10, and sent through an absorption cell where its concentration was measured (2.0×10^{16} molecules/cm^3) using a pen-ray Hg lamp (VWR Scientific, West Chester, PA) and a calibrated, UV sensitive photodiode (Edmund Scientific, Tonawanda, NY). After the absorption cell, O_3 entered the rear of the flow tube through a 0.44 cm i.d. moveable injector via an additional 24.1 sccm argon flow. Upon entering the flow tube, O_3 was further diluted by the particle flow so that the concentration of O_3 to which particles were exposed during reaction was 5.9×10^{14} molecules/cm^3 (24 ppmv, constant within 10%). Because this concentration is in considerable excess over the oleic acid concentration in the particle flow, the ozone concentration is essentially constant over the interaction distance. The pseudo first order conditions were ensured by keeping the oleic acid concentration below 0.4 ppmv, thereby providing a sixty fold excess of O_3.

The particle flow was split at the end of the flow tube with 330 sccm entering the aerodynamic lens of the aerosol mass spectrometer, and the remaining 480 sccm being either pumped away or directed to the aerodynamic particle sizer (APS Model Number 3321, TSI Inc., Shoreview, MN) where the particle size distribution was monitored. The reaction terminated once the particles entered the aerodynamic lens where the pressure dropped to 4.0 mbar. The range of interaction times for this 1 m flow tube, including time spent in the 0.2" i.d. tube connecting the flow tube to the aerodynamic lens inlet, was 1 to 23 seconds.

The particles that entered the aerodynamic lens[48,49] through the 200 μm nozzle were focused to the center of a 2 mm aperture, where they were accelerated by gas expansion into the vacuum chamber. The particles traveled 30 cm through two stages of differential pumping and arrived in the source region of a time of flight mass spectrometer (TOF-MS). Operation of the TOF-MS has been described in previous studies[29,50], so only a brief

summary will be provided here. Particle velocities, and thus arrival times in the ionization region, were determined by detecting scattered light from two green, continuous diode laser beams located between the second differentially pumped stage and the TOF-MS vaporization/ionization chamber. The photomultiplier (PMT) signals were sent into a timing circuit, which sent separate voltage pulses to trigger the flash lamps and Q-switch of a Nd:YAG laser.[51] The laser was fired to intersect the arrival of the particle vapor plume created by impinging the particles on a cartridge heater. Production of 118 nm vacuum UV light (10.5 eV photons) resulted from frequency tripling the 355 nm output of a Nd:YAG laser in a Xe (20 mbar)/Ar (200 mbar) gas cell by accessing a virtual energy state slightly to the blue of the $5d^3P_1$ state of Xe. Ions were accelerated into the flight tube with a pulsed extraction field, where they were collected by a pair of multichannel plates. Each firing of the VUV laser resulted in a complete single particle mass spectrum on a digital oscilloscope (HP, Infinium, Palo Alto, CA), which was transferred to a PC. In order to increase the precision and accuracy of the measurement, 100 single particle mass spectra were averaged. Figure 3.2 shows example mass spectra taken for oleic acid (MW 282)/myristic acid (MW 228) particles with a myristic acid mole fraction, $X_{MA} = 0.03125$. Similar mass spectra were collected at various reaction times. Measurements were made at 290K for pure particles and those over a range of myristic acid mole fractions ($X_{MA} = 0.03125$, 0.0625, 0.125, 0.25, and 0.35).

Unreacted particles were collected and imaged by both scanning electron and light microscopy. In preparation for SEM, dry particles were collected on glass cover slips that were attached to conductive carbon strips, mounted on Al studs. The sample was then sputter coated with Au/Pd and imaged.[52] For light microscopy, samples were collected on

a glass slide, and images were acquired via digital camera within an hour after particle collection. SEM images were collected within two hours of particle collection.

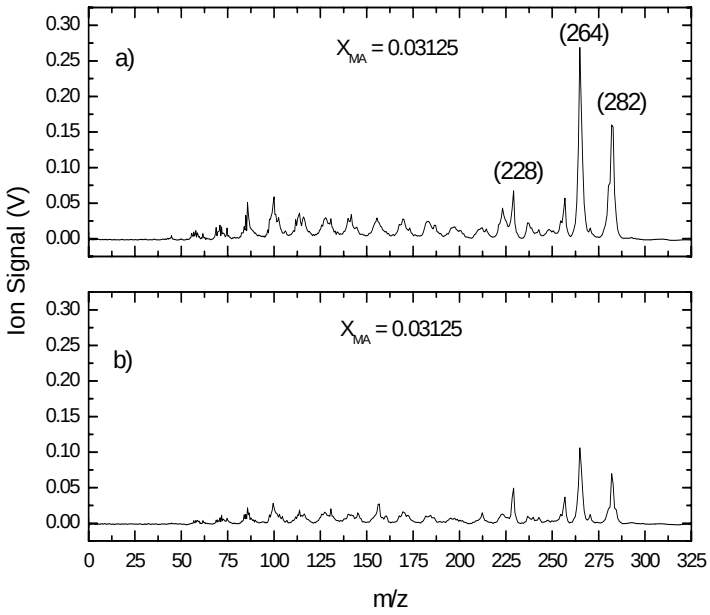

Figure 3.2: TOF-MS of a) a X_{MA} = 0.125 particle at t_{rxn} = 0.9 sec. (m/z 282) represents the parent peak of oleic acid, (m/z 264) represents water loss from oleic acid, (m/z 228) is the myristic acid parent peak, and (m/z 155) is OH loss peak of 9-oxononanoic acid (an oleic acid ozonlysis product). b) a X_{MA} = 0.125 particle at t_{rxn} = 20.12 sec

3.3 Results and Discussion

A typical oleic acid decay due to ozonolysis is shown in Figure 3.3 for X_{MA} = 0.03125. A pseudo first order rate constant for oleic acid depletion can be found from the slope of ln([oleic]/[oleic]$_0$) vs. time, where [oleic]/[oleic]$_o$ is the ratio of the m/z 282 oleic acid parent peak area after some reaction time to the m/z 282 peak area for unreacted particles. It should be kept in mind however, that the oleic acid can decay not only by ozonolysis, but also by reaction with stabilized Criegee intermediates (SCIs, Figure 3.4) that are produced from ozonolysis.[53] SCIs react with acids to produce hydroperoxy esters,[54]

which cause oleic acid concentrations to decay faster than from ozonolysis alone. Although the myristic acid is not attacked by ozone,

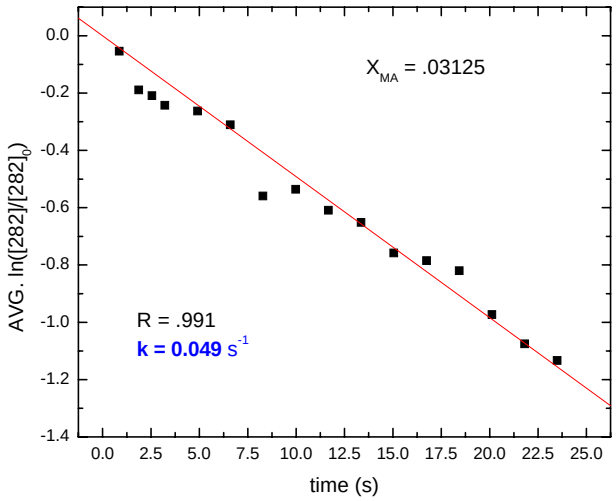

Figure 3.3: Oleic acid decay profile for a 2 μm, X_{MA} = 0.03125 mixed particle. Profiles were plotted according to ln([oleic]/[oleic]$_0$), where [oleic]/[oleic]$_o$ comes from the parent peak (m/z 282) of oleic acid.

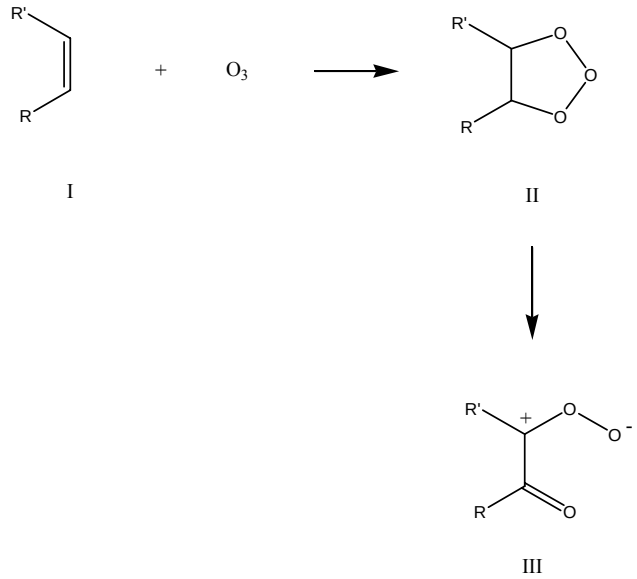

Figure 3.4: The formation of a stabilized Criegee intermediate (SCI). I:Alkene, II: primary ozonide, III: SCI

its acid group also reacts with SCIs.[55] The extent to which the SCI reacts with the acid is an interesting question that cannot be determined by studying the reaction of pure oleic acid and ozone unless both the decrease in ozone and oleic acid are monitored. However, the SCI/acid reaction can be followed by monitoring the decrease in the myristic acid concentration. In the course of this analysis, it became clear that the data are consistent only with a mechanism in which 100% of the SCI react with either oleic or myristic acid. The following mechanism was thus used to analyze the data:

$$oleic + O_3 \xrightarrow{k_1} SCI$$

$$oleic + SCI \xrightarrow{k_o} products \tag{3.1}$$

$$myristic + SCI \xrightarrow{k_m} products$$

The steady state approximation was made for SCI, yielding the following concentration:

$$[SCI]_{ss} = \frac{k_1[oleic]}{k_o[oleic] + k_m[myristic]} \tag{3.2}$$

The expression for $[SCI]_{ss}$ was then used to obtain the ratio between k_o and k_m in terms of the ratio of the reaction rates of oleic acid and myristic acid according to the following derivation:

$$\frac{-d[oleic]}{dt} = k_1[oleic] + k_o[oleic][SCI] = k_1[oleic] + \frac{k_1 k_o[oleic]^2}{k_o[oleic] + k_m[myristic]} \tag{3.3}$$

$$\frac{-d[myristic]}{dt} = k_m[myristic][SCI] = \frac{k_1 k_m[myristic][oleic]}{k_o[oleic] + k_m[myristic]} \tag{3.4}$$

where [SCI] has been replaced with the steady state concentration from equation 3.2. Taking the ratio of (3.3) and (3.4):

$$\frac{d[oleic]}{d[myristic]} = \frac{2k_o[oleic]}{k_m[myristic]} + 1 \tag{3.5}$$

allows us to solve for k_o/k_m in terms of the initial rates and initial concentrations:

$$\frac{k_o}{k_m} = \frac{\left(\left(\frac{d[oleic]_0}{d[myristic]_0}\right) - 1\right)[myristic]_0}{2[oleic]_0} \tag{3.6}$$

The ratios of these reaction rates as a function of the myristic acid mole fraction are shown in Figure 3.5.

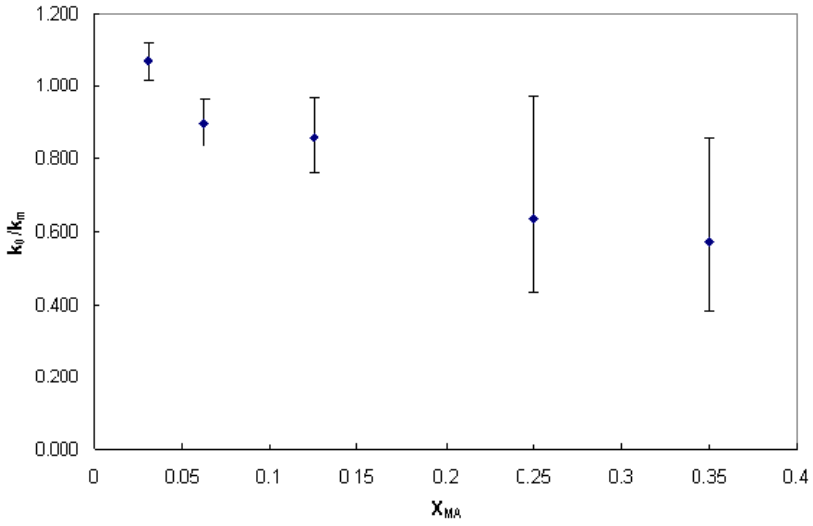

Figure 3.5: k_o/k_m as a function of X_{MA}.

Within the error of the myristic acid reaction rate determination, this k_o/k_m ratio is near 1. The nearly equal reaction rate with the SCI is not unexpected in view of the fact that myristic acid and oleic acid differ in length by only four carbons. The larger error in k_o/k_m for high X_{MA} is a result of the larger scatter in myristic acid decay curves at these particle compositions. Scatter in the myristic acid decay for these partially solid particles could be due to deviations in particle shape[56] or imperfect heater geometry.[57] Given k_o/k_m ~1,

$n_{oleic,avail}$, the number of oleic acid molecules in a particle available for ozonolysis, can be calculated according to:

$$n_{oleic,avail} = \left(1 - \frac{\left(1 - X_{MA}\right)}{2}\right) n_{oleic,particle} \tag{3.7}$$

where $n_{oleic,particle}$ is the total number of oleic acid molecules in a particle of a given composition. This equation is derived based on the above mechanism and takes into account our finding that 100% of the SCIs react with the acid groups. This finding is contrast to the results of Hearn *et al.*[58] who found that only 36% of the SCIs react with the acid group. Hearn *et al.* derived this value on the basis of studies with mixtures of oleic acid and methyl oleate, in which the ester group was immune to attack by the SCI. We do not understand the origin of the discrepancy in these two results unless, perhaps they are related to the fact that the Hearn *et al.* particles remained liquid throughout, whereas the present particles are partially solid.

The number of available oleic acid molecules can be used to calculate the ozone uptake coefficient for its reaction with oleic acid. The uptake coefficient represents the probability that a gas-aerosol particle collision results in the destruction of an ozone molecule, and is given by:

$$\gamma = \frac{\text{reaction rate}}{\text{collision rate}} = \frac{k_1 \, n_{oleic,avail}}{\left(\frac{\pi \bar{c} d^2}{4}\right) \rho_{O_3}} \tag{3.8}$$

where k_1 is the observed pseudo first order rate constant, $n_{oleic,avail}$ is the number of oleic acid molecules in an aerosol particle available for ozonolysis, $\bar{c}$ is the mean kinetic speed of O_3 molecules in the gas phase (cm/s), d is the particle diameter (cm), and ρ_{O3} is the density of ozone expressed in molecules/cm^3.[24,59]

Figure 3.6 is a plot of the uptake coefficient versus particle composition. For a pure oleic acid particle, γ is 3.4 ($\pm$ 0.3) x 10^{-4}. The γ determined in our study for liquid particles after correcting for the role of the SCI + oleic acid reaction is within a factor of 3 of values determined by coated wall flow tube studies[45,44] and the Hearn *et al.* study[58], where the latter also accounted for the contribution of the SCI + oleic acid reaction. Note that the uptake coefficient is independent of the particle size, which ranged from 200 nm[28] to 2 μm used in this study, as expected from the proposed model of oleic acid droplet reactivity.[60] Below X_{MA} = 0.125 the reactivity of mixed oleic acid/myristic acid particles is representative of a liquid particle, with dilution reducing the reaction rate of oleic acid.

At X_{MA} = 0.125, γ drops sharply to 9.7 ($\pm$ 1.0) x 10^{-5}. The mole fraction at which the reactivity decreases corresponds nicely with the X_{MA} at the crystallization point of an oleic acid/myristic acid mixture at 290 K.[47] In related studies, supercooling has been invoked for mixed particles for which the particle appeared to remain liquid well past the crystallization point.[46,24,44] In all of these studies, the uptake coefficient drops abruptly when crystallization commences.

What causes this drop in reactivity? For a pure liquid oleic acid particle, the diffuso-reactive length, the distance an ozone molecule diffuses before it reacts, is represented by the following expression:

$$\lambda = \sqrt{\frac{D}{k[oleic]}} \tag{3.9}$$

where ℓ is the diffuso-reactive length, D is the diffusion constant of ozone in oleic acid and k is the first order rate constant. Using an estimated value of D, we find ℓ = 18 nm, which is in good agreement with previous work.[29] Dilution of oleic acid with myristic acid should

result in an *increased* diffuso-reactive length because the reduced oleic acid concentration means that ozone needs to diffuse further into the particle in order to react. This dilution effect is shown as a solid line through the data points in Figure 3.6. Before the sharp drop off in γ, $X_{MA} = 0$ was used as the reference from which dilution was calculated. The calculated dilution line after the γ drop off used $X_{MA} = 0.125$ as the reference. Within our experimental uncertainty, the values of the

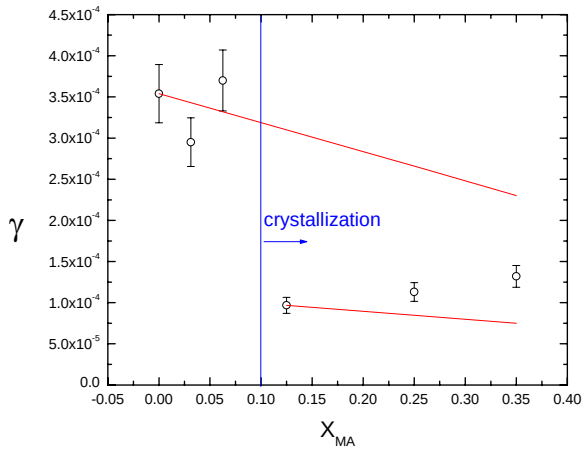

Figure 3.6: Reactive uptake coefficient as a function of X_{MA}. Note the drop off in γ at the myristic acid crystallization point.

uptake coefficients before and after crystallization are consistent with dilution. Reduction in the diffusion coefficient due to myristic acid crystallization leads to a *decrease* in this length, effectively reducing ozone accessibility to oleic acid. Therefore, decreased diffusivity at the crystallization point leads to a dramatic decrease in reactivity, while dilution reduces the reaction rate in a predictable way.[31]

Now let us consider the formation of a solid phase in more detail. The two-component oleic/myristic acid phase diagram[47] exhibits a eutectic point at $X_{MA} = 0.090$ at a temperature of 284 K. At the 290 K temperature of our study, a myristic acid solid phase

will form for $X_{MA} > 0.10$. However, in this equilibrium system, the amount of solid phase will be very small with the bulk being a solution enriched in oleic acid. That is, at $X_{MA} = 0.125$ only 2.5% of the reaction mixture (but 20% of the myristic acid) will be solid. Yet our experiment indicates that γ drops by a factor of 3.5, which seems too large an effect for such a small solid phase. On the basis of their SEM images of reacted stearic acid/oleic acid particles, Katrib *et al*.[24] suggested that the mixed particles consist of a solid stearic acid phase in the center of the particle, surrounded by a liquid layer. However, with this morphology, a γ similar to that of an uncrystallized particle would be expected because the oleic acid would remain exposed to ozone. On the other hand, if in our case, myristic acid were to reside on the surface of the particle, as is expected for micelle like structures[61,62], the reactivity would decrease dramatically because of the decreased mass transfer across this surface. Note that only 1% of the reaction mixture would be required for one monolayer to cover the entire surface of the particle. The crystalline surface would, in fact, be a bilayer consisting of either an outer myristic acid monolayer and an ordered, inner oleic acid layer or two myristic acid layers. Because myristic acid has no double bonds, it can form a denser and less permeable outer layer than is possible for the cis isomer of oleic acid.

In order for this proposed myristic acid bilayer to account for the drop in reactivity, the diffusion constant for ozone through this layer would have to drop significantly. The characteristic diffusion time, t, in a particle is given by:[1]

$$t = \frac{d^2}{\pi^2 D_l} \tag{3.10}$$

d is the particle diameter (cm), and D_l is the liquid phase diffusion coefficient. The oleic acid self diffusion constant is 3×10^{-7} cm^2/s, so that the diffusion time for a 1 micron particle would be about 3 ms, which is much shorter than the reaction time in the flow tube. In order

for the diffusion time to drop to 3 seconds (which is the time scale of the flow tube experiment), and assuming a bilayer thickness of 20 nm, the diffusion coefficient would have to be on the order of 10^{-13}, which is a four order of magnitude drop in diffusivity relative to pure oleic acid.

An outer layer of crystalline myristic acid nicely explains the sharp drop in the uptake coefficient with only 2% of the reaction mixture in the solid phase. But, the essentially constant γ after crystallization and the continued reactivity of the myristic acid after crystallization must also be explained. The essentially constant γ at $X_{MA} > 0.12$ rules out an increasingly thick crystalline myristic acid layer on the outside, because this would result in a continued sharply decreasing uptake coefficient as the myristic acid concentration increases. The particle morphology after crystallization must keep both the oleic and the myristic acids readily available for reaction with ozone. This means that if the myristic acid solid phase continues to grow as X_{MA} increases, it must be rather non-crystalline and porous, quite unlike the ordered outer layer phase.

An alternative explanation for the constant reactivity past the crystallization point would be incomplete coverage of the surface where the liquid oleic acid would be interspersed amongst the islands of crystalline myristic acid, the latter covering approximately 75% of the surface. Then these islands would grow deeper rather than wider with increasing myristic acid concentrations. Unfortunately, the quality of the images (discussed below) does not allow us to discern between these two possibilities.

The drop in reactivity when the crystal structure first forms is in contrast to the findings of Hearn and Smith[46] who found evidence for supercooled particles that yielded liquid like uptake coefficients well past the crystallization point of their oleic / myristic acid

mixtures. In their study, they prepared the sample by homogeneous nucleation and cooled the particle to the temperature of their flow tube experiment. However, when they lowered the temperature first and then brought the particles back up to the flow tube temperature, the particles had the lower γ values characteristic of solid particles.

The difference in the present results and those of Hearn and Smith may well be a result of sample preparation, which may lead to different polymorphs.[63,64] Polymorphs, which are solids that share chemical composition with another material but are composed of a different crystal lattice, are quite common among fats and lipids, and were specifically found for the case of saturated and unsaturated fatty acids.[65] In our work, aerosols are produced by an atomizer, and the propanol solvent evaporates from the surface. Evidently, the method used in the present experiment, does not lead to supercooling but rather to the thermodynamically favored phase, in which the outer layer is crystalline. As evaporation would tend to cool the particles to a significant degree,[66] the crystallization would lead to a different polymorph than those particles prepared by homogeneous nucleation. Because a kinetically favored (but thermodynamically less stable) polymorph may result from homogeneous nucleation, it may be that this crystal phase resides in the bulk rather than at the surface, in contrast to our results. In part, this explains the supercooling phenomenon. If the crystals form in the bulk, one would not expect to see a significant decrease in reactivity until a significant portion of the particle was in the form of crystallized myristic acid, exactly what Hearn and Smith's results show. Cooling of the particles would then cause the transformation of one polymorph into the most stable surface covered structure.

Images of our particles taken with a scanning electron microscope are shown in Figure 3.7. Figure 3.7a shows a spherical liquid particle, before reaction and with X_{MA} =

0.03125. Here the low contrast of the liquid particles made images difficult to obtain. Figure 3.7b shows unreacted crystallized particles at X_{MA} = 0.25. The brightness of the partially crystallized particles, which made the images easy to obtain, comes from Bragg diffraction resulting from the increased order of the crystalline phase.[67,68,69,70,71] These images stand in contrast to those reported by Katrib *et al*.[24] which were found to be needle like. They also provided evidence of super cooling of their oleic/stearic acid particles. Yet, their method of particle preparation is identical to the one reported here, namely propanol evaporation. Stearic acid, as opposed to myristic acid, has a monotectic point at the pure oleic acid composition, and should immediately solidify in oleic acid at room temperature.[72] Despite this difference, we do not expect that the saturated

a) 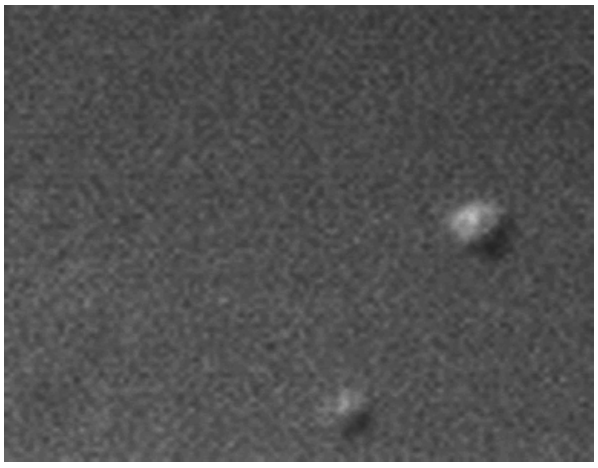

b) 

Figure 3.7: a) Image of liquid myristic acid/oleic acid particle (X_{MA} = 0.03125) taken with a scanning electron microscope (SEM) (29800x magnification) before ozonolysis. b) Image of crystallized myristic acid/oleic acid particle (X_{MA} = 0.35) taken via SEM (29800x magnification) before ozonolysis.

stearic and myristic acids, the latter being four carbon atoms shorter, should behave significantly different.[47] It is thus difficult to understand how different polymorphs may result. There are evidently subtle factors involved in determining how a component of a particle crystallizes. Further investigations are needed to resolve this issue.

3.4 Conclusions

Reactivity of mixed oleic acid and myristic acid particles has been studied in a flow tube apparatus using single particle mass spectrometry. It was found that the particle reactivity decreased according to dilution. However, past the crystallization point, a marked decrease in reactivity was observed. While these results agree with some previous work, the reactivity of these particles does not show any effect of supercooling as in other work. The formation of a myristic acid surface layer explains how as little as 20% "solid" myristic acid can cause a factor of 3 decrease in the ozone uptake coefficient. The diffusion rate of ozone

through this layer would have to be four orders of magnitude less than the diffusion rate in liquid oleic acid.

The findings of this study demonstrate the complicated effect that particle morphology has on the reactivity of its constituents. Phase transitions occur on short time scales and are sensitive to temperature and pressure changes. For example, a change in a few degrees results in a crystallized particle. This is important with respect to how much of the remaining liquid phase material will be available for reaction, and the extent to which that reactivity will be diminished.

Acknowledgements

We thank the National Science Foundation for financial support. We also thank Dr. Robert Bagnell from the department of Pathology and Laboratory Medicine at UNC for help with obtaining SEM images. Finally, we thank Professors Sergei Sheiko and Edward Samulski for insightful discussions.

References

[1] B. J. Finlayson-Pitts, J. N. Pitts, Chemistry of the Upper and Lower Atmosphere: Theory, Experiments and Applications, Academic Press, New York, NY 2000.

[2] J. E. Penner, M. Andrea, H. Annegarn, L. Barrie, J. Feichter, D. Hegg, A. Jayaraman, R. Leaitch, D. Murphy, J. Nganga, G. Pitari, in: B. Nyenzi, J. Prospero (Eds.), Climate Change 2001: The Scientific Basis. Contribution of Working Group I to the Third Assessment Report of the Intergovernmental Panel on Climate Change (IPCC), Cambridge University Press, Cambridge, 2001.

[3] P. R. Buseck, M. Posfai, Proceedings of the National Academy of Sciences of the United States of America, 1999, 96, 3372.

[4] V. Ramanathan, P. J. Crutzen, J. T. Kiehl, D. Rosenfeld, Science 294 (2001) 2119.

[5] V. Ramaswamy, O. Boucher, J. Haigh, D. Hauglustaine, J. Haywood, G. Myhre, T. Nakajima, G. Y. Shi, S. Solomon, in: F. Joos, J. Srinivasan (Eds.), Climate Change 2001: The Scientific Basis. Contribution of Working Group I to the Third Assessment Report of the Intergovernmental Panel on Climate Change (IPCC), Cambridge University Press, Cambridge, 2001.

[6] C. A. Stroud, P. A. Makar, D. V. Michelangeli, M. Mozurkewich, D. R. Hastie, A. Barbu, J. Humble, Environ.Sci.Technol. 38 (2004) 1471.

[7] K. E. Broekhuizen, T. D. Thornberry, P. P. Kumar, J. P. D. Abbatt, J.Geophys.Res. 109 (2004) D24206.

[8] T. Novakov, J. E. Penner, Nature 365 (1993) 823.

[9] T. Novakov, C. E. Corrigan, Geophys.Res.Lett. 23 (1996) 2141.

[10] K. E. Huff Hartz, J. E. Tischuk, M. N. Chan, C. K. Chan, N. M. Donahue, S. N. Pandis, Atmos.Environ. 40 (2006) 605.

[11] J. Kaiser, Science 307 (2005) 1858.

[12] D. H. Rivero, S. R. Soares, G. Lorenzi-Filho, M. Saiki, J. J. Godleski, L. Antonangelo, M. Dolhnikoff, P. H. Saldiva, Toxicological Sciences 85 (2005) 898.

[13] T. Heistracher, W. Hofmann, I. Balásházy, J.Appl.Physiol. 94 (2003) 1719.

[14] D. Loomis, M. Castillejos, D. R. Gold, W. McDonnell, V. H. Borja-Aburto, Epidemiology 10 (1999) 118.

[15] J. L. Quay, W. Reed, J. Samet, R. B. Devlin, American journal of respiratory cell and molecular biology 19 (2006) 98.

[16] S. L. Zeger, F. Dominici, J. Samet, Epidemiology 10 (2006) 171.

[17] D. W. Dockery, C. A. I. Pope, Ann.Rev.Public Health 15 (1994) 107.

[18] D. W. Dockery, C. A. I. Pope, X. Xu, J. D. Spengler, J. H. Ware, M. E. Fay, B. G. Ferris, F. E. Speizer, New Engl.J.Med. 329 (1993) 1753.

[19] A. P. Prishivalko, Zhurnal Prikladnoi Spektroskopii 33 (1980) 351.

[20] G. B. Ellison, A. F. Tuck, V. Vaida, J.Geophys.Res. 104 (1999) 11633.

[21] Y. Rudich, Chem.Rev. 103 (2003) 5097.

[22] J. H. Seinfeld, J. F. Pankow, Ann.Rev.Phys.Chem. 54 (2003) 121.

[23] M. C. Jacobson, H. C. Hansson, K. J. Noone, R. J. Charlson, Reviews of Geophysics 38 (2000) 267.

[24] Y. Katrib, G. Biskos, P. R. Buseck, P. Davidovits, J. T. Jayne, M. Mochida, M. E. Wise, D. R. Worsnop, S. T. Martin, J.Phys.Chem.A 109 (2005) 10910.

[25] C. N. Cruz, S. N. Pandis, J.Atmos.Chem. 31 (1997) 2205.

[26] K. G. Sexton, H. E. Jeffries, M. Jang, R. M. Kamens, M. Doyle, I. Voicu, Inhalation Toxicology 16 (2004) 107.

[27] K. B. Leach, R. M. Kamens, 2 (1997) 782.

[28] J. W. Morris, P. Davidovits, J. T. Jayne, Q. Shi, C. E. Kolb, D. R. Worsnop, W. S. Barney, J. Jimenez, G. R. Cass, Geophys.Res.Lett. 29 (2002) 71/1.

[29] G. D. Smith, E. Woods III, C. Hauser, R. E. Miller, T. Baer, J.Phys.Chem.A 106 (2002) 8085.

[30] J. D. Hearn, G. D. Smith, J.Phys.Chem.A 108 (2004) 10019.

[31] P. J. Ziemann, Faraday Discuss. 130 (2005) 1.

[32] W. F. Rogge, M. A. Mazurek, L. M. Hildemann, G. R. Cass, B. R. T. Simoneit, Atmos.Environ. 27A (1993) 1309.

[33] W. F. Rogge, L. M. Hildemann, M. A. Mazurek, G. R. Cass, B. R. T. Simoneit, Environ.Sci.Technol. 25 (1991) 1112.

[34] L. M. Hildemann, M. A. Mazurek, G. R. Cass, B. R. T. Simoneit, Environ.Sci.Technol. 25 (1991) 1311.

[35] J. F. Hamilton, P. J. Webb, A. C. Lewis, J. R. Hopkins, S. Smith, P. Davy, Atmos.Chem.and Phys. 4 (2004) 1279.

[36] D. A. Lake, M. P. Tolocka, M. V. Johnston, A. S. Wexler, Environ.Sci.Technol. 37 (2003) 3268.

[37] M. P. Tolocka, P. A. Solomon, W. Mitchell, G. A. Norris, D. B. Gemmill, R. W. Wiener, R. W. Vanderpool, J. B. Homolya, J. Rice, Aerosol Sci.Technol. 34 (2001) 88.

[38] L. S. Hughes, J. O. Allen, P. Bhave, M. J. Kleeman, G. R. Cass, D. Y. Liu, D. P. Fergenson, B. D. Morrical, K. A. Prather, Environ.Sci.Technol. 34 (2000) 3058.

[39] L. S. Hughes, J. O. Allen, M. J. Kleeman, R. J. Johnson, G. R. Cass, D. S. Gross, E. E. Gard, M. E. Gaelli, B. D. Morrical, D. P. Fergenson, T. Dienes, C. A. Noble, D. Y. Liu, P. J. Silva, K. A. Prather, Environ.Sci.Technol. 33 (1999) 3506.

[40] M. Jang, B. Carroll, B. Chandramouli, R. M. Kamens, Environ.Sci.Technol. 37 (2003) 3828.

[41] M. Jaoui, K. G. Sexton, R. M. Kamens, Atmos.Environ. 38 (2004) 2709.

[42] R. M. Kamens, M. W. Gery, H. E. Jeffries, M. Jackson, E. I. Cole, Int.J.Chem.Kin. 14 (1982) 955.

[43] J. J. Schauer, W. F. Rogge, L. M. Hildemann, M. A. Mazurek, G. R. Cass, B. R. T. Simoneit, Atmos.Environ. 30 (1995) 3837.

[44] D. A. Knopf, L. M. Anthony, A. K. Bertram, J.Phys.Chem.A 109 (2006) 5579.

[45] T. Moise, Y. Rudich, J.Phys.Chem.A 106 (2002) 6469.

[46] J. D. Hearn, G. D. Smith, Phys.Chem.Chem.Phys. 7 (2005) 2549.

[47] T. Inoue, Y. Hisatsugu, R. Ishikawa, M. Suzuki, Chem.Phys.Lipids 127 (2004) 161.

[48] P. Liu, P. J. Ziemann, D. B. Kittelson, P. H. McMurry, Aerosol Sci.Technol. 22 (1995) 293.

[49] P. Liu, P. J. Ziemann, D. B. Kittelson, P. H. McMurry, Aerosol Sci.Technol. 22 (1995) 314.

[50] C. Sykes, E. Woods III, G. D. Smith, T. Baer, R. E. Miller, Anal.Chem. 73 (2001) 2048.

[51] E. R. Mysak, Y. N. Dessiaterik, C. J. McKinney, R. E. Miller, T. Baer, Rev.Sci.Instrum. 77 (2006) 013301.

[52] J. I. Goldstein, D. E. Newbury, P. Echlin, D. C. Joy, C. Fiori, E. Lifshin, Scanning Electron Microscopy and X-Ray Microanalysis: a text for biologists, materials scientists, and geologists, Plenum Press, New York, NY, 1981.

[53] M. E. Jenkin, S. M. Saunders, M. J. Pilling, Atmos.Environ. 31 (1997) 81.

[54] P. Bailey, Ozonation in Organic Chemistry, Academic Press, 1978.

[55] M. A. Dreyfus, M. P. Tolocka, S. M. Dodds, J. Dykins, M. V. Johnston, J.Phys.Chem.A 109 (2005) 6242.

[56] H. J. Tobias, P. M. Kooiman, Docherty K.S., P. J. Ziemann, Aerosol Sci.Technol. 33 (2000) 170.

[57] J. T. Jayne, D. C. Leard, X. Zhang, P. Davidovits, K. A. Smith, C. E. Kolb, D. R. Worsnop, Aerosol Sci.Technol. 33 (2000) 49.

[58] J. D. Hearn, A. J. Lovett, G. D. Smith, Phys.Chem.Chem.Phys. 7 (2005)

[59] M. P. Tolocka, T. D. Saul, M. V. Johnston, J.Phys.Chem.A 108 (2004) 2659.

[60] C. E. Kolb, D. R. Worsnop, M. S. Zahniser, P. Davidovits, T. R. Keyser, M. T. Leu, M. J. Molina, D. R. Hanson, A. R. Ravishankara, in: J.R. Barker (Ed.), Progress and Problems in Atmospheric Chemistry: Current problems in Atmospheric Chemistry, 1995, p.771.

[61] M. Iwahashi, Y. Kasahara, H. Matsuzawa, K. Yagi, K. Nomura, H. Terauchi, Y. Ozaki, M. Suzuki, J.Phys.Chem.B 104 (2000) 6186.

[62] E. Sloutskin, X. Z. Wu, T. B. Peterson, O. Gang, B. M. Ocko, E. B. Sirota, M. Deutsch, Physical Review E 68 (2003) 031605.

[63] T. Sonoda, Y. Takata, S. Ueno, K. Sato, Crystal Growth and Design 6 (2006) 306.

[64] S. Ueno, Y. Hamada, K. Sato, Crystal Growth and Design 3 (2006) 935.

[65] K. Sato, N. Yoshimoto, T. Arishima, J.Dispersion Science and Technology 10 (1989) 363.

[66] W. C. Hinds, Aerosol Technology: Properties, Behavior, and Measurement of Airborne Particles, Wiley Interscience, New York, NY, 1982.

[67] B. J. Krueger, V. H. Grassian, A. Laskin, J. P. Cowin, Geo.Res.Lett. 30 (2003) 48-1.

[68] H. X. Chen, R. A. Dobbins, Combust.Sci.Technol. 159 (2000) 109.

[69] R. A. Dobbins, R. A. Fletcher, W. Lu, Combust.Flame 100 (1995) 301.

[70] B. Oktem, M. P. Tolocka, B. Zhao, H. Wang, M. V. Johnston, Combust.Flame 142 (2005) 364.

[71] R. A. Fletcher, R. A. Dobbins, H. C. Chang, Combust.Flame 115 (1998) 285.

[72] T. Inoue, H. Yusuke, Y. Reiri, S. Masao, Chemistry and physics of lipids 127 (2004) 143.

CHAPTER 4

Technical Aspects

4.1 Introduction

This chapter focuses on detailed aspects of operating and optimizing the performance of the aerosol mass spectrometer. Among these are the introduction of particles into the aerosol mass spectrometer, alignment of diode lasers with the particle beam to obtain size and velocity information, and alignment of the vaporization and ionization lasers with the particle beam for efficient particle detection and analysis.

4.2 Aerodynamic Lens Alignment

The aerodynamic lens system, shown in Figure 4.1, consists of a series of concentric disks. The diameter of the aperture in these disks decreases along its axis (d = 0.197, 0.189, 0.177, 0.169, and 0.157"). This serves to focus incoming aerosol particles into a beam as described by Liu *et al.*[1,2] The principle of the lens is based on the fluid dynamics of the particles as they negotiate their way around these apertures. The particles traveling with a flowing gas experience a drag force shown in equation (4.1).

$$F_D = \frac{C_D \pi \rho_m d^2 v^2}{8} \tag{4.1}$$

where C_D is the drag coefficient which describes the flow regime (i.e. turbulent, laminar, intermediate) around a particle, ρ_m is the density of the medium in which the particles are traveling, d is the particle diameter, and ν is

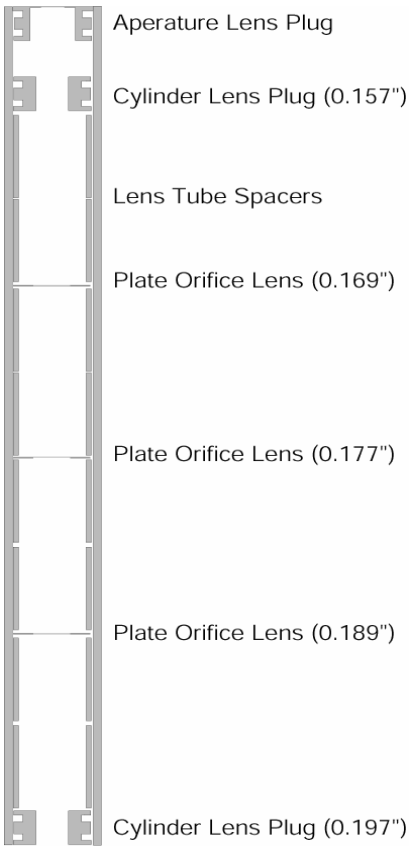

Figure 4.1: Schematic of aerodynamic lens assembly (Not to scale)

the velocity difference between the particle and the surrounding gas. A particle with the optimal diameter for a given lens size and flow conditions will pass through the lens and be focused closer to the central axis of the aerodynamic lens system. Whether or not the particle is focused closer to the central axis of the aerodynamic lens system after passing through a given single lens depends on its mass. Particles which are too small will follow the gas streamlines exactly and be the same distance from the central axis both before and after going through a given lens. Particles that are too large will have a large amount of momentum and impact on the front of the lens or be defocused. Particles in an optimum size range as determined by flow conditions and lens geometry will cross gas streamlines on their way through the lens and have enough momentum to remain near the central axis after passing through. Example particle trajectories for each of these cases is shown in Figure 4.2.

Alignment of the aerodynamic lens is critical to ensuring that aerosol particles strike the cartridge heater (*ca.* 6 mm diameter) located in the main chamber of the TOF-MS. The first step in this process is to align the aerodynamic lens so that the beam from a HeNe laser can be sent through the aerodynamic lens, two skimmers, as well as the particle light scattering region and ultimately strike the cartridge heater. This is done with the entire instrument open to atmosphere. The HeNe beam simulates the path of an aerosol beam traveling through the instrument. Next, a glass slide covered with vacuum grease is attached to the cartridge heater, the flow limiting orifice is placed in the entrance to the aerodynamic lens system, and the instrument is placed under vacuum. Salt particles are produced either via nebulizer (Meinhard, Golden, CO) or constant output atomizer (TSI Inc., Shoreview, MN), swept through a drying tower with argon, and sent into the aerodynamic lens where they are focused into a particle beam. Particles are sent into the instrument for *ca.* 1 hr and

collected on the glass slide attached to the heater. After the collection period, the TOF-MS instrument

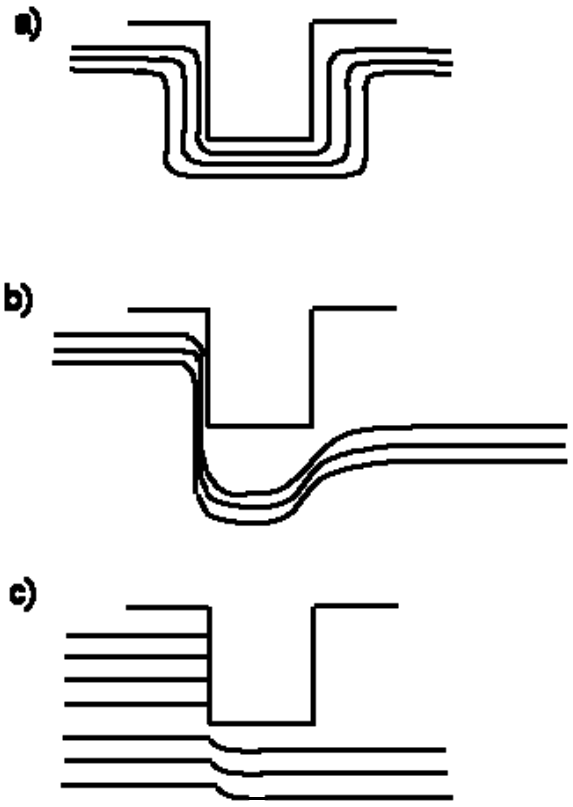

Figure 4.2[3]: Particle trajectories through a single lens for a) very small particles that follow gas streamlines and remain unfocused b) particles in the optimum size range for focusing and thus move closer to the lens central axis and c) particles too large for focusing that impact upon the lens surface

is again open to atmosphere, and the location of the HeNe laser beam spot on the glass slide can then be compared to the location of the *ca.* 2 mm spot made by the collected salt particles. The process can then be repeated while making fine adjustments to the position of the aerodynamic lens, until the spot made by the collected particles overlaps the HeNe beam spot. This iterative process is necessary because in order for the HeNe spot to be bright

enough to see when it reaches the heater; it is aligned through the instrument with the 200 μm flow limiting orifice removed from the aerodynamic lens. Therefore, the aerodynamic lens may require slight adjustment to center the particle beam on the heater. After each particle collection period, the flow limiting orifice is removed to verify that both the particle beam and HeNe are hitting the heater and overlap with each other.

4.3 Particle Detection

Optimizing particle detection involves diode laser alignment and the aforementioned particle beam alignment that results from aligning the aerodynamic lens system. The light scattering set up used in these experiments can be seen in the schematic shown in Figure 4.3. In this system, particles cross two green, cw diode lasers separated by 10 cm and oriented perpendicularly to the particle beam. Scattered light from each diode laser is detected by a photomultiplier tube (PMT) oriented at a 30° angle from the plane formed by the intersecting diode laser and particle beams.

Particles that have diameters on the order of the wavelength of incident radiation are described according to Mie theory calculations (Figure 4.4a). The intensity of scattered light according to this theory is represented by equations 4.2a-c:

$$I_{up} = \frac{I_0 \lambda^2 (f(\theta, m, d_p)_\perp + f(\theta, m, d_p)_\parallel)}{8\pi^2 r^2} \tag{4.2a}$$

$$I_\perp = \frac{I_0 \lambda^2 f(\theta, m, d_p)_\perp}{4\pi^2 r^2} \tag{4.2b}$$

$$I_\parallel = \frac{I_0 \lambda^2 f(\theta, m, d_p)_\parallel}{4\pi^2 r^2} \tag{4.2c}$$

where I_{up}, $I_{\perp}$, and $I_{\parallel}$ represent the intensities of scattered light from unpolarized, perpendicularly polarized, and parallel polarized incoming radiation. Additionally, λ represents the wavelength of the incident radiation, r represents the particle to detector distance, and f is a complicated function of scattering angle (θ), index of refraction (m), and particle diameter (d_p). A plot of $f(\theta, m, d)$ vs. scattering angle is shown in Figure 4.5. The maximum for this function is at 0°. The scattering pattern is relatively smooth for k = 0.8 and 2, but becomes more complicated for larger k values such as k = 10. In Figure 4.5, 30° is near one of the valleys in the scattering pattern for k = 10. However, the scattering intensity for this k value is still at least an order of magnitude larger than for k = 2. Therefore, 30° is a good angle to collect scattered light, providing a balance between collecting at a small angle in order to detect light from the smallest possible particles, and collecting from an angle which is too small and allowing for the detection of non-scattered light. As particles become smaller, with diameters on the order of the wavelength of incoming radiation, their scattered light intensity can be described by Rayleigh scattering, a limiting case of Mie theory. Equations describing scattering in the Rayleigh region are as follows:

$$I_{up} = \frac{\pi^4 N d_p^{\,6}}{8\lambda^4 r^2}\left|\frac{m^2-1}{m^2+2}\right|\left(1+\cos^2\theta\right)I_0 \tag{4.3a}$$

$$I_{\parallel} = \frac{\pi^4 N d_p^{\,6}}{8\lambda^4 r^2}\left|\frac{m^2-1}{m^2+2}\right|\left(\cos^2\theta\right)I_0 \tag{4.3b}$$

$$I_{\perp} = \frac{\pi^4 N d_p^{\,6}}{8\lambda^4 r^2}\left|\frac{m^2-1}{m^2+2}\right| I_0 \tag{4.3c}$$

where θ is the angle between incoming radiation and the detector. All other variables are as defined in equations 4.2a-c. According to Rayleigh scattering, if the particle diameter

decreases by a factor of 10, the intensity of scattered light detected at a given angle is reduced by a factor of 10^6. This makes it extremely difficult to detect particles less than ~ 500 nm in diameter in our case. Some instruments[4,5] employ elliptical mirrors, which allow collection of scattered light from many angles, to extend the range of particle sizes that can be detected.

The first step in aligning the diode lasers is to pass a HeNe laser through the TOF-MS while open to atmosphere, as done for the aerodynamic lens alignment. This simulates the path traveled by the particle beam. Next, a small container of dry ice is placed in the light scattering region. The HeNe and diode laser beams can be seen by blowing a small amount of compressed air over the dry ice. Using this method, small adjustments can be made to the position of the diode lasers until they are observed to intersect the HeNe beam.

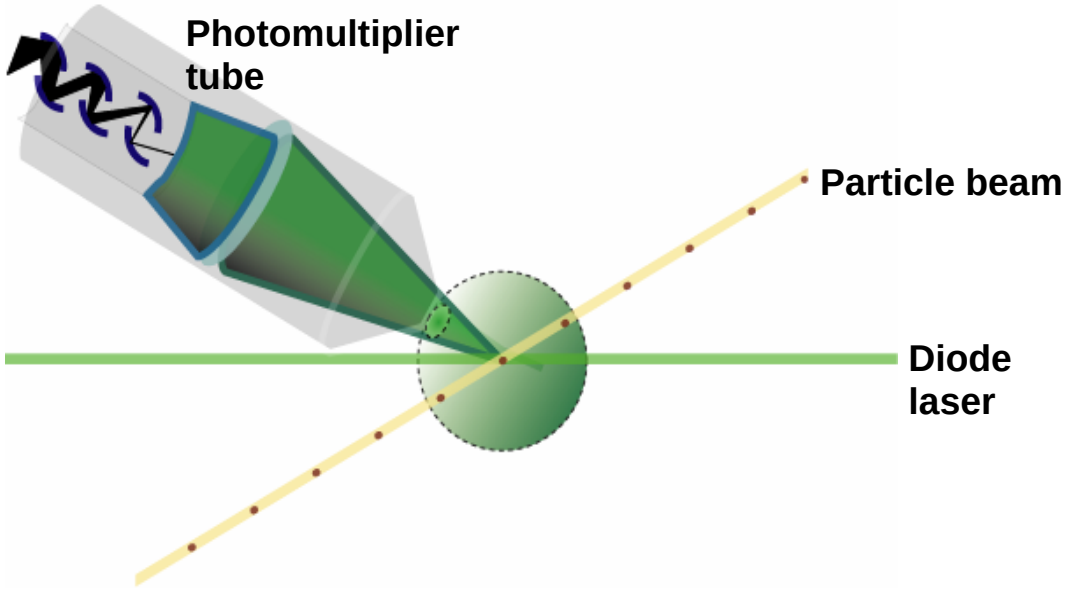

Figure 4.3: A schematic of a light scattering station in the TOF-MS

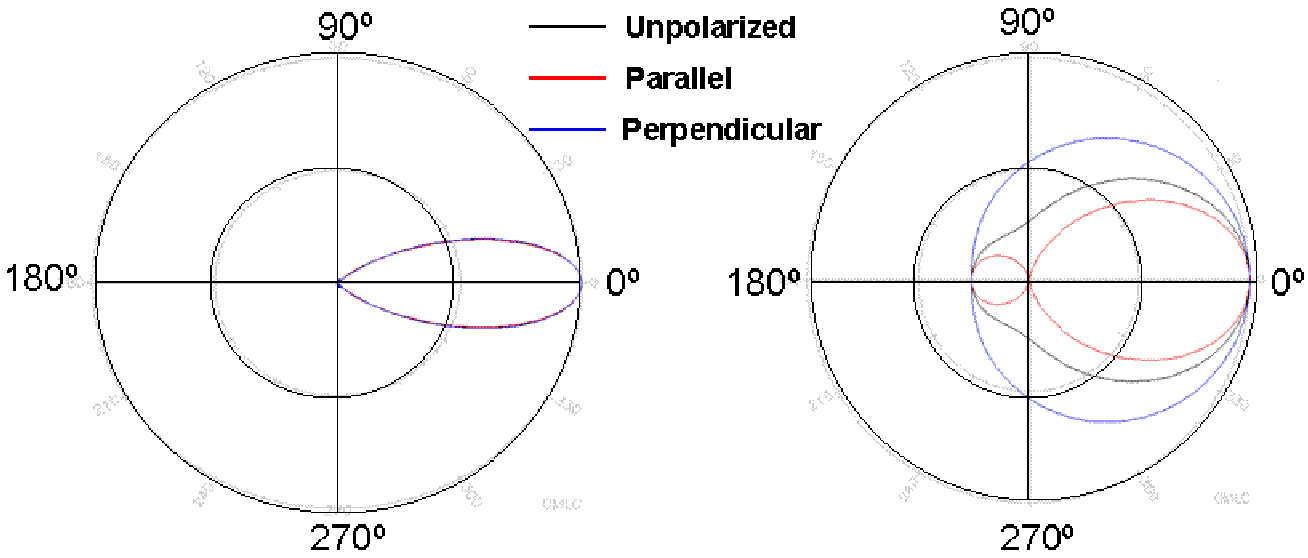

a) b)

Figure 4.4[6]: a) Polar plot of normalized Mie scattering intensity for a 700 nm particle scattering light from a λ = 532 nm diode laser. b) Polar plot of normalized Mie scattering intensity for a 200 nm diameter particle scattering light from a λ = 532 nm diode laser.

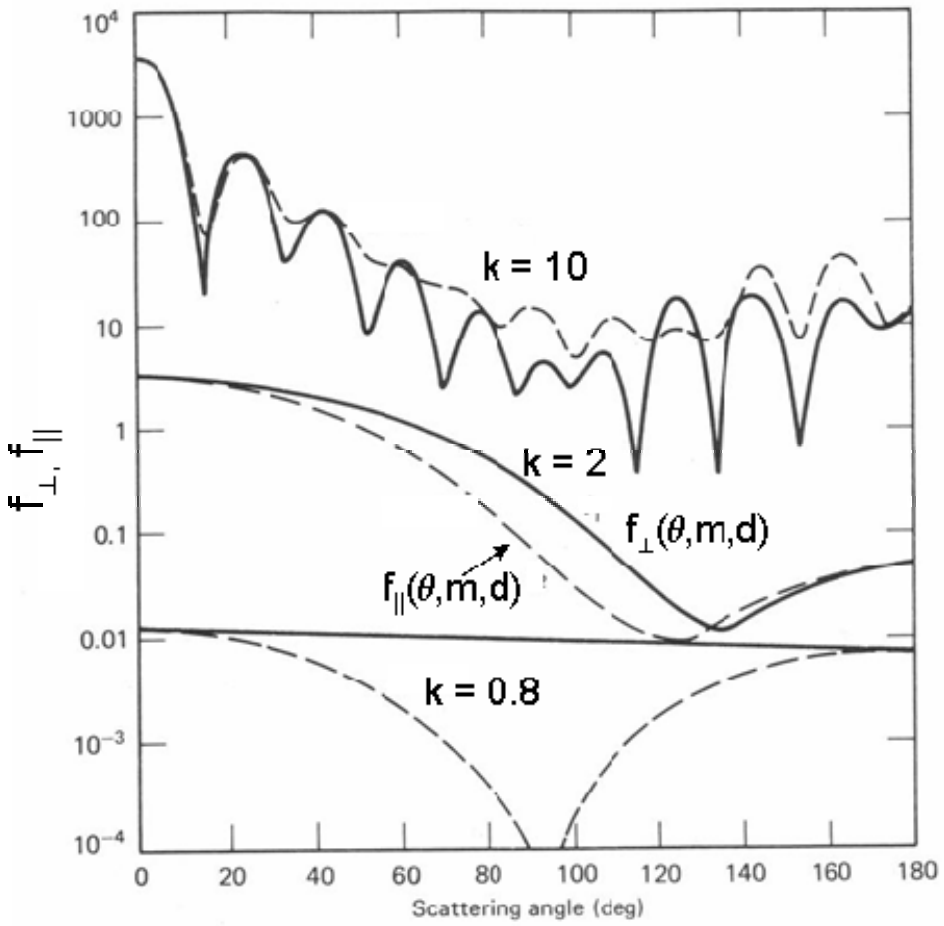

Figure 4.5: f(θ, m, d) vs. scattering angle[7] The solid line represents the value of f for perpendicularly polarized light and the dashed line represents values of f for parallel polarized light. k is referred to as a size parameter and is defined as: $\frac{\pi d_p}{\lambda}$, where d_p is the particle diameter, and λ is the wavelength of incident radiation. In the figure above, k = 10, 2, and 0.8 correspond to d_p = 1.7 μm, 339 nm, and 135 nm respectively.

The next step is to evacuate the system, followed by introduction of aerosol particles. The need for further fine adjustment of diode laser position can be determined through observation of the raw PMT signal at each scattering station. An example of the raw PMT signal for a 2 μm diameter particle is shown in Figure 4.6. Ideally, if particles are properly focused in the aerodynamic lens, and if both diode lasers are aligned equally well, the frequency with which particles scatter light at each PMT will be the same. In an experiment,

the time between scattering events is used to determine particle velocity, and thus diameter. Salt *et al.* have shown this method has a smaller standard deviation than determining particle sized based solely on the intensity of the scattered light signal.[8]

4.4 Particle Detection Efficiency

Once both the particle beam and the diode lasers are aligned, it is necessary to quantitatively determine the particle detection efficiency to determine a baseline for optimal instrument performance. The set up for the efficiency measurements is shown in Figure 4.7. Polystyrene latex spheres (PSLs) (Duke Scientific, Fremont, CA) diluted with a 50:50 ethanol:water mixture by volume were nebulized (Meinhard, Golden, CO) into a drying tower where the ethanol:water mixture was evaporated by a flow of argon. The particle flow was split at the exit of the drying tower, with 330 sccm entering the aerodynamic lens system, and the remaining flow either being directed to the aerodynamic particle sizer (APS model number 3321, TSI Inc., Shoreview, MN) or pumped away. As with the instrument in this lab, particles cross and scatter light from two separate laser beams in the APS. As opposed to this instrument, the APS uses elliptical mirrors to collect the scattered light and focus it onto a photomultiplier. The time difference between electrical pulses received at each scattering station is then used to determine the particle's aerodynamic diameter. The APS also determines both total particulate concentration and the concentration of individual size bins.

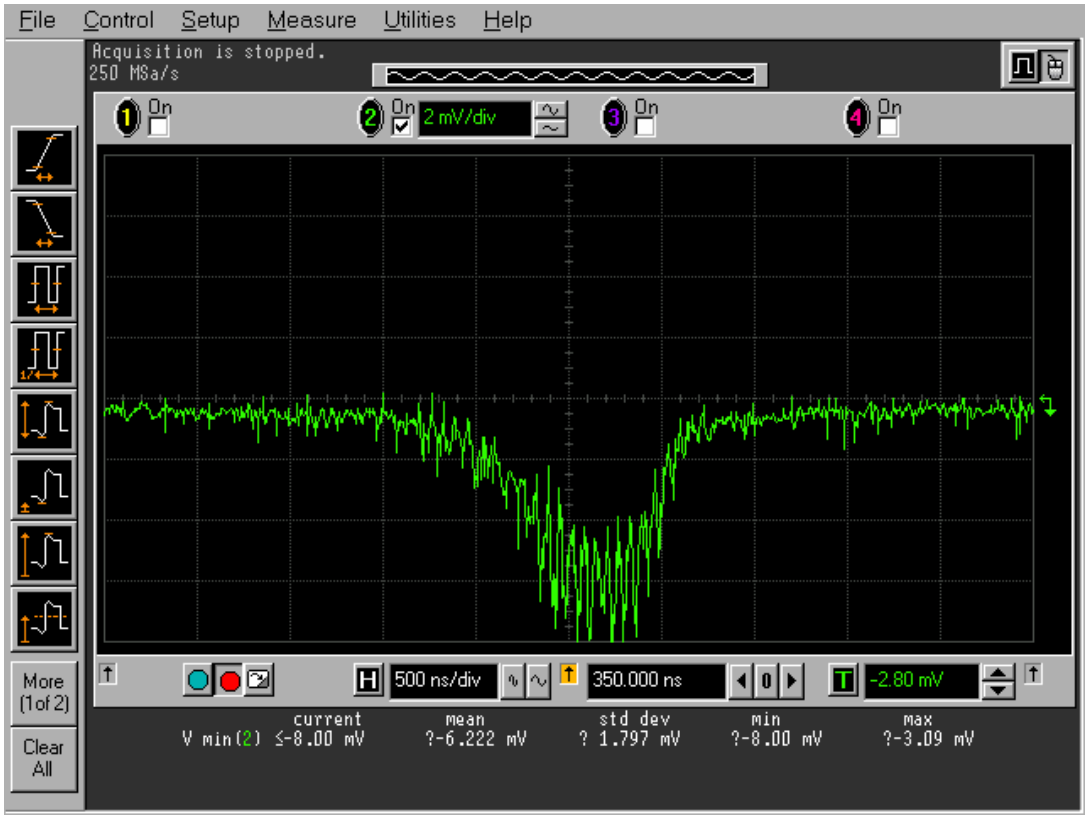

Figure 4.6: Raw PMT signal for a 2 μm PSL sphere. FWHM *ca.* 750 ns.

Therefore, the first step in determining particle detection efficiency was to record a particle size distribution over a period of *ca.* 10 minutes, as determined by the light scattering set-up of the aerosol mass spectrometer. A size distribution was also recorded with the APS approximately every 2.5 minutes during this collection period. Using the APS distributions, an average particle concentration was calculated for the PSL sphere diameter of interest. Given the flow through the 200 μm limiting orifice, the rate that particles enter the instrument was calculated according to:

$$F = nc \tag{4.4}$$

where F is the particle flux (particles/sec) through the orifice, n is the particle concentration (particles/cm^3), and c is the conductance (4 cm^3/sec) of the 200 μm orifice. The number of particles that are detected by the two diode lasers in the aerosol MS instrument are then determined by collecting the particle velocity distribution. This yields both the vacuum aerodynamic size distribution as well as the rate of particles entering the MS. The efficiency of particle introduction into the aerosol MS is then given by:

$$E = \frac{F_{aerosolMS}}{F_{calc}} \tag{4.5}$$

where E is the detection efficiency, $F_{aerosolMS}$ is the aerosol MS instrument particle detection rate (particles/sec), and F_{calc} is the theoretical particle detection rate calculated with the APS size distributions and inlet flow. The result of an efficiency determination is shown in Figure 4.8, and serves as a baseline for instrument performance and is comparable to detection efficiencies obtained by Allen *et al.*[9], with the exception of the point at $D_p = 0.76$ μm. One possibility for such poor detection efficiency at this particle diameter is a partially plugged flow limiting orifice. If this were the case when 0.76 μm particles were examined, the particle trajectories may have been altered, thereby affecting their detection.

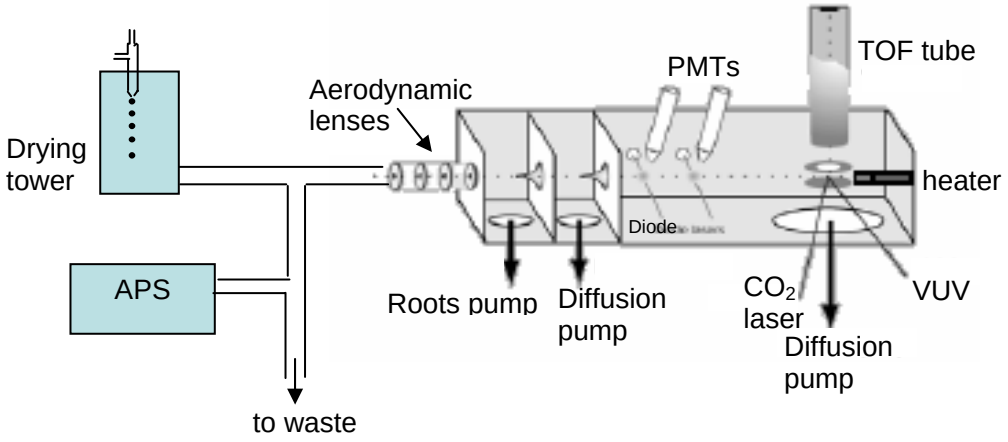

Figure 4.7: Schematic of set-up for particle transmission efficiency determination (Not to scale)

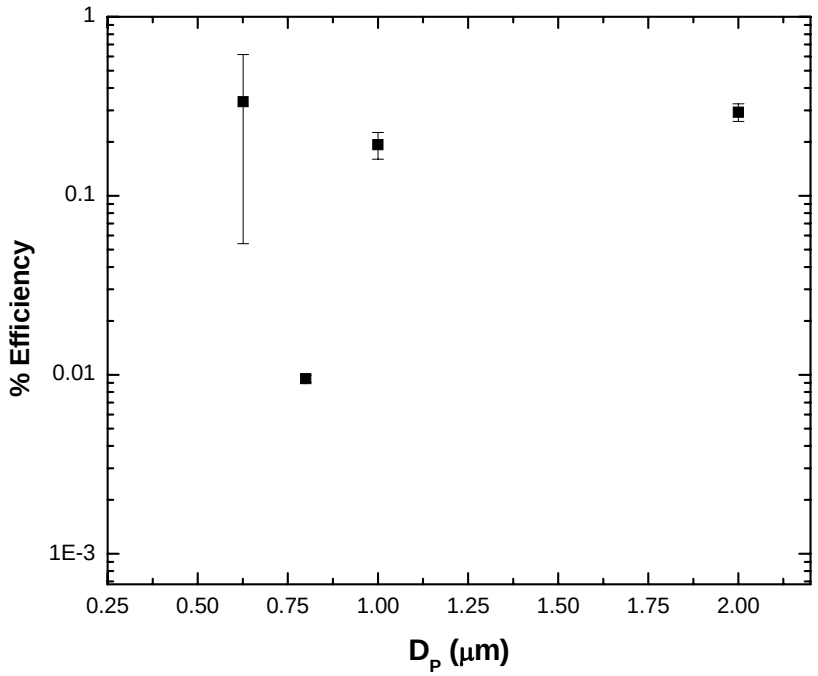

Figure 4.8: Measured particle transmission efficiency for PSL spheres of varying diameter

4.5 Vaporization/Ionization Laser Alignment

In order to maximize mass spectral signal, it is necessary to ensure that the vaporization and ionization lasers are properly aligned. A schematic of the set-up for laser entrance into the TOF-MS is shown in Figure 4.9. For this process, it is preferable to first line up the CO_2 vaporization laser. The first step in this process is to situate a HeNe laser on the side of the TOF-MS where the CO_2 laser beam exits the instrument after having passed through the interaction region. The HeNe laser is then used to simulate the path taken by the CO_2 laser beam by adjusting the optics used to steer the CO_2 laser such that the HeNe beam strikes it. This provides a rough initial alignment. Further modification can be made by imaging the IR beam on a graphite detector and following its path to the instrument. Finally, in order to fine tune the CO_2 laser alignment, particles are introduced into the TOF-MS. To optimize vertical alignment, particles are introduced into the instrument at a rate greater than 10 Hz so that a nearly continuous particle beam exists. Particles used in this case are composed of a salt such as NaCl or RbCl dissolved in an ethylene glycol/isopropanol mixture. This eliminates the need for a VUV ionization laser as Na^+ or Rb^+ ions in solution are liberated upon particle vaporization, extracted by a DC field, and detected by the MCPs. The position of the CO_2 laser beam is then vertically adjusted until the intensity of the mass spectral signal is optimized.

Next, the vaporization efficiency, or the ratio of the number of particles vaporized to the number of CO_2 shots fired, is optimized. The particle introduction rate is reduced to less than 10 per second, and the CO_2 laser is triggered by the electronic unit that signals the arrival time of a particle in the ionization region. This is done by scanning the delay time between when the particle arrival time and the laser trigger pulse.

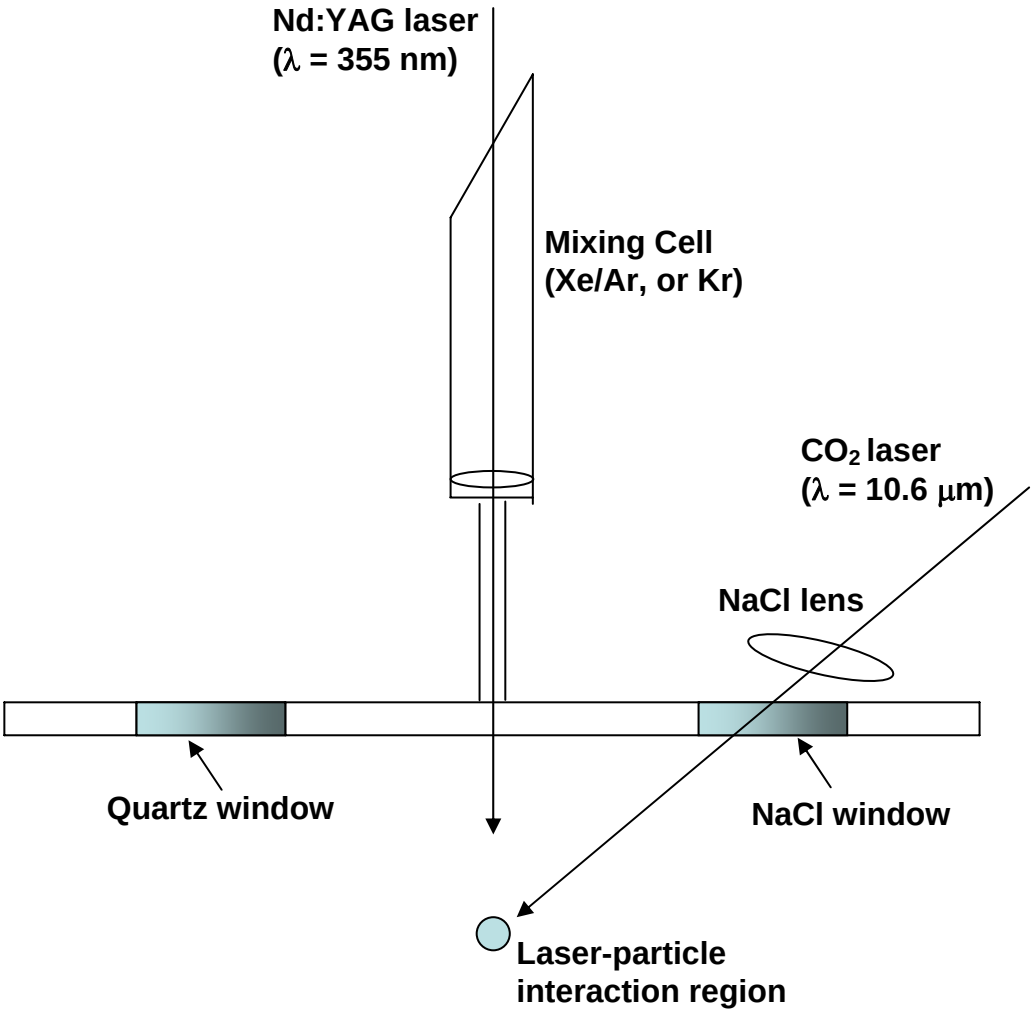

Figure 4.9: Schematic (not to scale) of laser introduction to the TOF-MS

A usual spatial separation between the CO_2 laser pulse and the VUV laser pulse in the interaction region is on the order of 1 mm. This is designed to account for the motion of the particle center of mass.[10] Given that this is the desired separation and that a typical particle travels through the TOF-MS at *ca.* 100 m/s, a reasonable CO_2-VUV delay time would be 10 μs, the time at which the particle center of mass would intersect the VUV laser

spot. However, one must account for the fact that this delay time will change depending upon the translational temperature of the resultant vapor plume.[10] For example, oleic acid molecules (MW = 282 g/mol) ejected with a translational temperature of 560 K have an average velocity of 205 m/s, and therefore an optimal delay of *ca.* 2.5 μs, given that the vapor plume travels both toward and away from the vaporization region. This optimal delay is for this specific case and will change with changing translational temperature or different CO_2-VUV spatial separation. In the case of VUV laser alignment, a particle such as oleic acid that does not yield an ion upon vaporization is used so that the VUV laser is isolated during this process.

References

[1] P. Liu, P. J. Ziemann, D. B. Kittelson, P. H. McMurry, Aerosol Sci.Technol. 22 (1995) 293.

[2] P. Liu, P. J. Ziemann, D. B. Kittelson, P. H. McMurry, Aerosol Sci.Technol. 22 (1995) 314.

[3] X. Zhang, K. A. Smith, D. R. Worsnop, J. Jimenez, J. T. Jayne, C. E. Kolb, Aerosol Sci.Technol. 36 (2002) 617.

[4] A. Zelenyuk, D. Imre, Aerosol Sci.Technol. 39 (2005) 554.

[5] E. Gard, J. E. Mayer, B. D. Morrical, T. Dienes, D. P. Fergenson, K. A. Prather, Anal.Chem. 69 (1997) 4083.

[6] http://omlc.ogi.edu/calc/mie_calc.html

[7] W. C. Hinds, Aerosol Technology: Properties, Behavior, and Measurement of Airborne Particles, Wiley Interscience, New York, NY 1982.

[8] K. Salt, C. A. Noble, K. A. Prather, Anal.Chem. 68 (1996) 230.

[9] J. O. Allen, D. P. Fergenson, E. E. Gard, L. S. Hughes, B. D. Morrical, M. J. Kleeman, D. S. Gross, M. E. Gaelli, K. A. Prather, G. R. Cass, Environ.Sci.Technol. 34 (2000) 211.

[10] E. Woods III, R. E. Miller, T. Baer, J.Phys.Chem.A 107 (2003) 2119.

CHAPTER 5

Conclusions/Future Directions

Throughout the course of this research, the vaporization and ionization methods used to analyze atmospheric aerosols have been studied. These studies have been paramount in understanding the effects that each method has on the fragmentation of organics, and the appearance of their mass spectra. These findings have been applied to studying the reactivity of particles composed of a binary mixture of oleic acid and myristic acid. In this study, particle reactivity due to changing morphology was examined, providing a look at particles more representative of typical tropospheric aerosols. Finally, methods used to examine and optimize instrument performance have been described as well.

It was observed that use of 10.6 μm IR radiation from a CO_2 laser led to inhomogeneous heating of particles. This was demonstrated by oleic acid mass spectra that are dependent on the CO_2/VUV laser delay time. This inhomogeneity made it impossible to discern the relative contribution of neutral dissociation and dissociative ionization to the fragmentation observed in oleic acid mass spectra. Vaporization using a cartridge heater provided a more homogeneous heating of the particles and thus relative mass spectral peaks that were invariant with delay of the ionization laser. In both cases, dissociation of oleic acid was shown to be slow on the timescale of the experiment by varying the time between ionization and ion extraction.

Reduction in the ionization photon energy led to a significant reduction in oleic acid fragmentation, resulting in a mass spectrum consisting of mainly parent (m/z 282) and water loss (m/z 264) peaks. This is a very important result for the field of aerosol mass spectrometry. Reduced fragmentation allows for the study of more complicated particles such as mixed or coated particles of the same size as pure particles that are studied, but where the amount of the analyte of interest is less. Of particular benefit would be the presence of a second dye laser, allowing for tunable photon energy. However, this does not lend to a portable set up which is the true goal of current aerosol mass spectrometry instrumental development. Another option being explored is the rare gas resonance lamp. These smaller lamps lend themselves to use with portable instruments.

An application of less fragmentation explored in this dissertation was the examination of the reactivity of mixed myristic acid/oleic acid particles with ozone in a flow tube. In this study, the uptake coefficient of ozone by oleic acid was shown to drop by a factor of 3.5 upon even minimal myristic acid crystallization. Contrary to similar studies on this subject, supercooling was not observed. Reduction of reactivity after crystallization of only 2.5% of the reaction mixture is explained by the formation of a myristic acid surface layer. Constant reactivity with increased crystallization beyond this point is hypothesized to be due to either formation of a surface myristic acid layer that is porous, or formation of "islands" of myristic on the particle surface. Unfortunately, SEM images do not provide a clear answer to this question, which warrants further study. This highlights the complexity of phase transitions and the reactivity of "real" aerosol particles.

A number of possible future studies have emerged from this work. Several questions still remain as to the exact structure of crystallized myristic acid in the mixed myristic

acid/oleic acid particles. A more thorough examination of crystal structure dependence on particle size would yield important understanding of this issue. Another interesting investigation would be a more thorough examination of particle reactivity as a function of particle preparation method. Varying the temperature at which particles are created and the manner in which they are subsequently cooled would also be important. In order to progress to analyzing even more complex particles, it is essential to pursue a more detailed understanding of these issues.